

# The LEGA-C and SAMI Galaxy Surveys: Quiescent Stellar Populations and the Mass–Size Plane across 6 Gyr

Tania M. Barone<sup>1,2,3\*</sup>, Francesco D’Eugenio<sup>4</sup>, Nicholas Scott<sup>2,3</sup>, Matthew Colless<sup>1,3</sup>, Sam P. Vaughan<sup>2,3</sup>, Arjen van der Wel<sup>4</sup>, Amelia Fraser-McKelvie<sup>3,5</sup>, Anna de Graaff<sup>6</sup>, Jesse van de Sande<sup>2,3</sup>, Po-Feng Wu (吳柏鋒)<sup>7</sup>, Rachel Bezanson<sup>8</sup>, Sarah Brough<sup>3,9</sup>, Eric Bell<sup>10</sup>, Scott M. Croom<sup>2,3</sup>, Luca Cortese<sup>3,5</sup>, Simon Driver<sup>5</sup>, Anna R. Gallazzi<sup>11</sup>, Adam Muzzin<sup>12</sup>, David Sobral<sup>13</sup>, Joss Bland-Hawthorn<sup>2,3</sup>, Julia J. Bryant<sup>2,3,14</sup>, Michael Goodwin<sup>15</sup>, Jon S. Lawrence<sup>15</sup>, Nuria P. F. Lorente<sup>15</sup>, Matt S. Owers<sup>16,17</sup>

<sup>1</sup>Research School of Astronomy and Astrophysics, The Australian National University, Canberra, ACT 2611, Australia

<sup>2</sup>Sydney Institute for Astronomy, School of Physics, The University of Sydney, NSW, 2006, Australia

<sup>3</sup>ARC Centre of Excellence for All Sky Astrophysics in 3 Dimensions (ASTRO 3D), Australia

<sup>4</sup>Sterrenkundig Observatorium, Universiteit Gent, Krijgslaan 281 S9, B-9000 Gent, Belgium

<sup>5</sup>International Centre for Radio Astronomy Research, The University of Western Australia, 35 Stirling Hwy, 6009 Crawley, WA, Australia

<sup>6</sup>Leiden Observatory, Leiden University, P.O.Box 9513, NL-2300 AA Leiden, The Netherlands

<sup>7</sup>National Astronomical Observatory of Japan, Osawa 2-21-1, Mitaka, Tokyo 181-8588, Japan

<sup>8</sup>Department of Physics and Astronomy and PITT PACC, University of Pittsburgh, Pittsburgh, PA 15260, USA

<sup>9</sup>School of Physics, University of New South Wales, NSW 2052, Australia

<sup>10</sup>Department of Astronomy, University of Michigan, 1085 S. University Ave., Ann Arbor, MI, 48109, USA

<sup>11</sup>INAF - Osservatorio Astrofisico di Arcetri, Largo Enrico Fermi 5, I-50125 Firenze, Italy

<sup>12</sup>Department of Physics and Astronomy, York University, 4700 Keele St., Toronto, Ontario, M3J 1P3, Canada

<sup>13</sup>Department of Physics, Lancaster University, Lancaster LA1 4YB, UK

<sup>14</sup>Australian Astronomical Optics - USyd, University of Sydney, NSW 2006, Australia

<sup>15</sup>Australian Astronomical Optics - Macquarie, Macquarie University, NSW 2109, Australia

<sup>16</sup>Department of Physics and Astronomy, Macquarie University, NSW 2109, Australia

<sup>17</sup>Astronomy, Astrophysics and Astrophotonics Research Centre, Macquarie University, Sydney, NSW 2109, Australia

Accepted XXX. Received YYY; in original form ZZZ

## ABSTRACT

We investigate the change in mean stellar population age and metallicity ( $[Z/H]$ ) scaling relations for quiescent galaxies from intermediate redshift ( $0.60 \leq z \leq 0.76$ ) using the LEGA-C Survey, to low redshift ( $0.014 \leq z \leq 0.10$ ) using the SAMI Galaxy Survey. We find that, similarly to their low-redshift counterparts, the stellar metallicity of quiescent galaxies at  $0.60 \leq z \leq 0.76$  closely correlates with  $M_*/R_e$  (a proxy for the gravitational potential or escape velocity), in that galaxies with deeper potential wells are more metal-rich. This supports the hypothesis that the relation arises due to the gravitational potential regulating the retention of metals, by determining the escape velocity required by metal-rich stellar and supernova ejecta to escape the system and avoid being recycled into later stellar generations. On the other hand, we find no correlation between stellar age and  $M_*/R_e^2$  (stellar mass surface density  $\Sigma$ ) in the LEGA-C sample, despite this being a strong relation at low redshift. We consider this change in the age– $\Sigma$  relation in the context of the redshift evolution of the star-forming and quiescent populations in the mass–size plane, and find our results can be explained as a consequence of galaxies forming more compactly at higher redshifts, and remaining compact throughout their evolution. Furthermore, galaxies appear to quench at a characteristic surface density that decreases with decreasing redshift. The  $z \sim 0$  age– $\Sigma$  relation is therefore a result of building up the quiescent and star-forming populations with galaxies that formed at a range of redshifts and so a range of surface densities.

**Key words:** galaxies: evolution – galaxies: fundamental parameters – galaxies: abundances – galaxies: structure – galaxies: stellar content – galaxies: statistics

## 1 INTRODUCTION

A challenge in the field of galaxy evolution is understanding the influence of redshift-dependent Universe conditions; i.e., how does

\* E-mail: tania.barone@anu.edu.au

the redshift at which a galaxy formed affect its evolutionary path? Galaxies observed at  $z \sim 0.76$  (nearly 7 Gyr lookback time) are remarkably different to those observed in the present-day Universe (e.g. Stott et al. 2016; van der Wel et al. 2016; Wisnioski et al. 2019). Compared to nearby galaxies at fixed stellar mass, at intermediate redshifts ( $z \sim 0.5\text{--}3$ ) galaxies are more compact (Ferguson et al. 2004; Trujillo et al. 2007; Buitrago et al. 2008; Williams et al. 2010; van der Wel et al. 2014; Mowla et al. 2019), more highly star-forming (with a peak in cosmic star formation density at  $z \approx 2$ ; Lilly et al. 1996; Madau et al. 1998; Daddi et al. 2007; Madau & Dickinson 2014), have dynamically hotter turbulent star-forming gas (Förster Schreiber et al. 2006; Weiner et al. 2006; Law et al. 2007; Förster Schreiber et al. 2009; Law et al. 2009; Wright et al. 2009; Wisnioski et al. 2011; Epinat et al. 2012; Swinbank et al. 2012; Kassin et al. 2012; Wisnioski et al. 2015), and higher molecular gas fractions (Tacconi et al. 2010; Daddi et al. 2010; Tacconi et al. 2013; Morokuma-Matsui & Baba 2015), indicating significant evolution over this time period. Crucially, galaxies today will not follow the same evolutionary path over the next 6 Gyr as similarly-massive galaxies that formed 6 Gyr ago (e.g. Barro et al. 2013; Abramson et al. 2016), because the conditions influencing evolutionary path change as the Universe evolves. The size difference between star-forming and quiescent galaxies is strong evidence for this change in evolutionary path. At fixed mass star-forming galaxies are larger than their quiescent counterparts (Kriek et al. 2009; Williams et al. 2010; Wuyts et al. 2011; van der Wel et al. 2014; Whitaker et al. 2017). While passive disk fading after ceasing star formation does lead to a decrease in effective radius, this process alone is insufficient to explain the size difference between the  $z = 0$  star-forming and quiescent populations (Croom et al. 2021b). Therefore, this difference in average size indicates that the star-forming progenitors of present day quiescent galaxies were different to the  $z \sim 0$  population of star-forming galaxies, which will instead evolve into extended quiescent galaxies (Barro et al. 2013). An alternative way of framing this is through ‘progenitor bias’ (van Dokkum & Franx 2001), which describes the bias that results from assuming that the evolutionary path followed by high-redshift galaxies to the present day will similarly be followed by low-redshift galaxies in the future.

Understanding the redshift dependence of galaxy evolution requires disentangling the evolution of an individual galaxy within a population, from the evolution in the average properties of the population as a whole (due to the continual addition of newly formed galaxies with different properties to the extant population). A key method of studying how both individual and populations of galaxies evolve is by analysing their growth in mass and size. An individual star-forming galaxy is expected to evolve along the relation of star-forming galaxies in the mass–size plane (Lilly et al. 1998; Ravindranath et al. 2004; Trujillo et al. 2006b; Pezzulli et al. 2015; van Dokkum et al. 2015), while the average size of the population as a whole increases with decreasing redshift due to new galaxies forming with larger radii (van Dokkum & Franx 2001; Carollo et al. 2013). In other words, star-forming galaxies at both low and intermediate redshifts follow parallel tracks in the mass–size plane (Speagle et al. 2014; van Dokkum et al. 2015), with their starting location in the plane depending on redshift. Therefore, when analysing star-forming galaxies in the mass–size plane at  $z \sim 0$ , we are observing the combined effect of both the evolution of individual galaxies throughout their lifetimes and the evolution of the population due to the addition of new members and loss of old members (as they quench). We want to disentangle these two effects to understand how the redshift range over which a galaxy formed and evolved influences its evolutionary path. We therefore need to understand how the processes influencing

a galaxy may be regulated by the broader conditions of the Universe and how these conditions change with redshift. An important tool to measure the impact of various processes is the analysis of scaling relations, which quantify the link between different galaxy parameters to determine their dependence. Specifically, scaling relations between stellar population parameters and galaxy structure allow us to quantify how processes involved in star-formation and stellar mass assembly interrelate with processes dominating structural and dynamical changes.

Recent studies analysing various stellar population scaling relations have demonstrated a clear dependence of stellar population and star formation history on galaxy size ( $R_e$ ), at both low and intermediate ( $z \sim 0\text{--}3$ ) redshifts (e.g., Bell et al. 2000; Bell & de Jong 2000; Kauffmann et al. 2003; van der Wel et al. 2009). Franx et al. (2008) investigated the dependence of  $u - g$  colour (interpreted as a proxy for star-formation history) on stellar mass ( $M_*$ ) and  $R_e$  for a sample spanning  $0 < z < 3$ . At all redshifts, they showed that  $M_*$  alone is not a good predictor of colour (and thus star-formation history), and that the correlations between  $u - g$  colour and  $M_*/R_e^2$  or  $M_*/R_e$  have less scatter than the relations with  $M_*$ . Wake et al. (2012) extended this work at low redshift ( $z < 0.11$ ), showing that  $u - r$  colour correlates more strongly with velocity dispersion ( $\sigma$ ) than  $M_*$ ,  $M_*/R_e^2$  or Sérsic index (Sérsic 1968). More recently, Díaz-García et al. (2019) used spectral energy distribution fits to optical and near-infrared photometry from ALHAMBRA (Advanced Large, Homogeneous Area Medium Band Redshift Astronomical Survey; Moles et al. 2008), to study how the stellar population properties of quiescent galaxies vary in the mass–size plane up to redshift  $z \sim 1$ . They found that stellar population properties show a dependence on galaxy mass and size since  $z \sim 1$ . Furthermore, low-redshift studies by McDermid et al. (2015), Scott et al. (2017) and Li et al. (2018) using spectroscopically-derived stellar population parameters showed that much of the scatter in the age– $M_*$  and metallicity– $M_*$  relations is due to residual trends with galaxy size, in that smaller galaxies at fixed mass are older and more metal rich. This difference in the resulting mean stellar population parameters can be traced back to differences in the star formation histories using simulations. Gupta et al. (2021) used the IllustrisTNG simulations (Pillepich et al. 2018) to track the evolution of extended massive galaxies and found that, compared to their normal-sized counterparts, extended galaxies quench later despite having similar star-formation rates and stellar masses when selected at  $z \sim 2$ . Furthermore, in addition to a dependence of global stellar population on galaxy structure, studies have also found a dependence *within* galaxies between local stellar population properties and local dynamical and structural parameters (e.g. González Delgado et al. 2014b, 2015; Møller & Christensen 2020; Zibetti et al. 2020), which suggests the global relations arise from local scales (Scott et al. 2009).

Barone et al. (2018, 2020, hereafter B18 and B20 respectively) built on these earlier studies by quantifying this observed dependence on size, and showing how global age and metallicity ( $[Z/H]$ ) correlate with the galaxy structure:  $M_*/R_e$  (a proxy for the gravitational potential,  $\Phi$ , or escape velocity<sup>1</sup>) and  $M_*/R_e^2$  (stellar mass surface density,  $\Sigma$ ) for low-redshift early-type and star-forming galaxies. Specifically, these studies quantified and compared the intrinsic scatter within each relation, and any residual trend with galaxy size.

<sup>1</sup> As shown by Scott et al. (2009) and Cappellari et al. (2013b), the difference between the escape velocities for the stellar body and the dark matter halo is not large ( $\sim 0.1$  dex), hence we can adopt  $M_*/R_e$  as a qualitative but reliable proxy for the potential well depth and escape velocity.)

Despite using different samples, methods, and models, the two studies found the same results in both early-type and star-forming galaxies: the correlations that are the tightest and have the least residual trend with galaxy size are the age– $\Sigma$  and  $[Z/H]$ – $M_*/R_e$  relations. Additionally, D’Eugenio et al. (2018) showed that gas-phase metallicity in star-forming galaxies at low redshift is also more tightly correlated with  $M_*/R_e$  than either  $M_*$  or  $\Sigma$ .

Based on these results, B18, B20 and D’Eugenio et al. (2018) proposed and discussed various mechanisms that could lead to the  $[Z/H]$ – $\Phi$  and age– $\Sigma$  relations. These studies concluded that the  $[Z/H]$ – $\Phi$  relation is driven by galaxies with low gravitational potentials losing more of their metals because the escape velocity required for metal-rich gas to be expelled by supernova feedback is directly proportional to the depth of the gravitational potential. Given this assumption, there should also exist a correlation between metallicity and gravitational potential at intermediate redshifts, although the slope and scatter of the relation may vary due to changes in the strength of star formation feedback and outflows. As for the age– $\Sigma$  relation, B20 proposed it results from compact galaxies having formed earlier than their diffuse counterparts, and so the mechanism(s) responsible for determining the size and mass of a galaxy at fixed age depend on redshift. This hypothesis is supported by the recent results of Díaz-García et al. (2019), who found that the formation epoch of quiescent galaxies since  $z \sim 1$  shows a strong dependence on size at fixed mass. The age– $\Sigma$  relation may therefore be less pronounced at intermediate redshifts, as less time has passed for the relation to build up. The aim of this paper is to test these hypotheses, by determining the redshift dependence of the age– $\Sigma$  and  $[Z/H]$ – $M_*/R_e$  scaling relations.

In this paper we build on the results of stellar populations scaling relations at low redshift by analysing if (and how) the relations change across a lookback time of 6 Gyr ( $0.014 \leq z \leq 0.76$ ), to test the hypotheses proposed for the age– $\Sigma$  and  $[Z/H]$ – $M_*/R_e$  scaling relations. Specifically, we study how the spatially-integrated average (global) age and metallicity of individual quiescent galaxies vary in the mass–size plane. Furthermore, we look at how the age– $\Sigma$  and  $[Z/H]$ – $M_*/R_e$  relations found at low redshift appear at  $0.60 \leq z \leq 0.76$ . By quantifying the significance of these scaling relations at low and intermediate redshift we aim to understand their origins and, in the process, begin to discern the redshift dependence of stellar population evolution over the past 6 Gyr.

The paper is arranged as follows. In Section 2 we describe the  $0.60 \leq z \leq 0.68$  and  $0.68 < z \leq 0.76$  samples from the LEGA-C survey and the  $0.014 \leq z \leq 0.10$  comparison sample from the SAMI survey. We address and quantify the size evolution of galaxies with redshift in our samples in Section 2.4 to ensure our results are not biased by this evolution. Section 3 describes the full spectral fitting method used to obtain the metallicity and age measurements, as well as the estimates of the uncertainties. We present our analysis methods and the  $[Z/H]$  and age results in Section 4. We then link our age– $\Sigma$  results to the distribution of the quiescent and star-forming populations across redshift in the mass–size plane in Section 4.3. We discuss the metallicity and age results in Section 5 and provide a summary of our conclusions in Section 6. We assume a flat  $\Lambda$  cold dark matter ( $\Lambda$ CDM) Universe with  $\Omega_\Lambda = 0.7$ ,  $\Omega_M = 0.3$  and  $H_0 = 70 \text{ km s}^{-1} \text{ Mpc}^{-1}$ , and a Chabrier (2003) initial mass function.

## 2 DATA

We describe the LEGA-C and SAMI surveys in Sections 2.1 and 2.2 respectively, followed by describing auxiliary measurements and the

sample selection in Section 2.3. In summary, the final samples consist of 1234 galaxies (553 quiescent and 681 star-forming) from the LEGA-C survey and 1176 galaxies (573 quiescent and 603 star-forming) from the SAMI survey. All galaxies lie within the mass range  $9.5 \leq \log(M_*/M_\odot) \leq 11.5$  and have a median signal-to-noise ratio (S/N) per  $\text{\AA} \geq 10$  in the rest-wavelength region 4427–4548 $\text{\AA}$ . We tested restricting the SAMI sample to  $10.0 \leq \log(M_*/M_\odot)$  to better match the stellar mass range of the LEGA-C quiescent galaxies and found the results are qualitatively unchanged. Therefore we present here the analysis with the larger sample size and mass range.

We restrict the stellar population analysis to quiescent galaxies because stellar population measurements of star-forming galaxies tend to have higher uncertainties and so require larger sample sizes to resolve underlying trends. This higher uncertainty arises for two main reasons. Firstly, the on-going star formation leads to strong ionised-gas emission that obscures absorption features containing stellar population information. Secondly, massive, short-lived stars are significantly brighter than low-mass, long-lived stars, and so a small population of recently-formed stars can outshine a much larger population of old stars, making it difficult to resolve the true underlying stellar distribution. Therefore, while we use both the quiescent and star-forming galaxies for the analysis of the mass–size plane (Section 4.3), we restrict the stellar population analyses to the quiescent population (see Section 2.3 for details on the adopted quiescent and star-forming classification).

Galaxies are well established to have internal radial stellar population gradients which, when combined with a varying aperture size, can lead to spurious global trends. A key difference between the two surveys are the apertures used; the VIMOS instrument used by LEGA-C is a slit spectrograph of 1" wide and 8" long, whereas the SAMI instrument uses fused-fibre hexabundles of 15" diameter, comprised of 61 individual fibres. For the SAMI targets we use spectra integrated within 1 effective radius ( $R_e$ ), and for the LEGA-C data we use spectra integrated along the entire slit. At  $z = 0.7$  1" corresponds to a physical scale of  $\sim 7.1$  kpc which encompasses at least 50% of the total flux. Therefore, despite the different apertures used in the two surveys, all galaxies are probed to at least  $1R_e$ , mitigating potential aperture bias when combining the two surveys. Furthermore, we are interested in how stellar population properties vary *within* redshift bins, which we then qualitatively compare between redshift bins. Therefore we only quantitatively compare galaxies within (not between) the two surveys.

### 2.1 The LEGA-C Survey

The Large Early Galaxy Astrophysics Census (LEGA-C; van der Wel et al. 2016) is a slit spectroscopic survey of galaxies at intermediate redshifts in the COSMOS field (Scoville et al. 2007), using the Visible Multi-Object Spectrograph (VIMOS; Le Fèvre et al. 2003) on the Very Large Telescope. The survey comprises 4209 galaxies, 3472 of which have spectroscopic redshift measurements within  $0.60 \leq z \leq 1.0$ . Targets were selected from the UltraVISTA catalogue (Muzzin et al. 2013a) and were observed for  $\sim 20$  hours to reach an approximate S/N per  $\text{\AA} \approx 20$  in the continuum. We use integrated spectra summed along the entire slit, with an effective spectral resolution of  $R \sim 3500$  (Straatman et al. 2018) and observed wavelength range  $\sim 6300\text{\AA} - 8800\text{\AA}$ . We use spectra from the third data release (van der Wel et al. in prep.); see van der Wel et al. (2016) and Straatman et al. (2018) for earlier data releases.

While the LEGA-C sample spans the redshift range  $0.60 \leq z \leq 1.0$ , above  $z \sim 0.8$  the survey selection criteria and the S/N requirement for stellar population analyses limit the sample to only the

brightest (most massive) targets. We therefore restrict our analysis to the redshift range  $0.60 \leq z \leq 0.76$ . Based on the estimate of the median size evolution from  $z = 0.60$  to  $0.76$  (Section 2.4), we further split the sample into two redshift bins,  $0.60 \leq z \leq 0.68$  and  $0.68 < z \leq 0.76$ .

## 2.2 The SAMI Galaxy Survey

The Sydney-AAO Multi-object Integral-field (SAMI; Bryant et al. 2015; Croom et al. 2021a) Galaxy Survey is a low-redshift integral-field survey of 3068 unique galaxies observed using the SAMI instrument (Croom et al. 2012) connected to the AAOmega spectrograph (Sharp et al. 2006, 2015) on the Anglo-Australian Telescope. The sample spans the redshift range  $0.004 \leq z \leq 0.11$ . Galaxies were observed through fused-fibre hexabundles (Bland-Hawthorn et al. 2011; Bryant et al. 2014), each comprising 61 tightly-packed fibres that form an approximately circular grid with a diameter of 15". Observations were typically for a total of 3.5 hours comprised of 7 dithers of 30 minutes each. Targets were selected based on stellar mass cuts in narrow redshift bins from three equatorial regions covered by the Galaxy And Mass Assembly (GAMA; Driver et al. 2011) survey and 8 cluster regions; see Bryant et al. (2015) and Owers et al. (2017) for a full description of the sample selection for the GAMA and cluster regions respectively. For this analysis we exclude targets from the cluster regions to avoid over-representing galaxies from dense environments. SAMI spectra have two components, a ‘blue’ component (3700–5700 Å) at a resolution of  $R=1800$ , and a ‘red’ component (6300–7400 Å) at  $R=4300$ . For the full-spectral fits the higher spectral resolution red component is degraded to match the resolution of the blue component. The whole spectrum is then fit simultaneously. We use spatially-integrated  $1R_e$  spectra from the third data release (Croom et al. 2021a)<sup>2</sup>; see Allen et al. (2015), Green et al. (2018) and Scott et al. (2018) for earlier releases.

## 2.3 Measurements of galaxy properties

Semi-major effective radii ( $R_e$ ) were measured from Sérsic fits using the GALFIT software (Peng et al. 2010). For LEGA-C targets the measurements followed the procedure of van der Wel et al. (2012) on HST ACS F814W images from the COSMOS program (Scoville et al. 2007) and for SAMI targets that of Kelvin et al. (2012), using  $r$ -band photometry from SDSS DR7 (Abazajian et al. 2009) reprocessed for GAMA (Hill et al. 2011).

We use stellar masses ( $M_*$ ) and star formation rates (SFR) measured with the MAGPHYS (Multi-wavelength Analysis of Galaxy Physical Properties da Cunha et al. 2008) spectral energy distribution fitting software by de Graaff et al. (2020, 2021) for the LEGA-C galaxies and Driver et al. (2018) for the SAMI galaxies. Both catalogues are derived using the Bruzual & Charlot (2003) library of synthetic stellar spectrum, a Charlot & Fall (2000) dust attenuation model and a Chabrier (2003) initial mass function. The two catalogues differ slightly in the photometric bands used for the fits due to differences in data availability, however they both include photometry ranging from ultra-violet to the far-infrared; see de Graaff et al. (2021) and Driver et al. (2018) for further details. We restrict both samples to galaxies with  $9.5 \leq \log(M_*/M_\odot) \leq 11.5$ , as outside these limits the samples become sparsely sampled and/or dominated by targets with low S/N.

In addition to covering the GAMA regions from which the SAMI

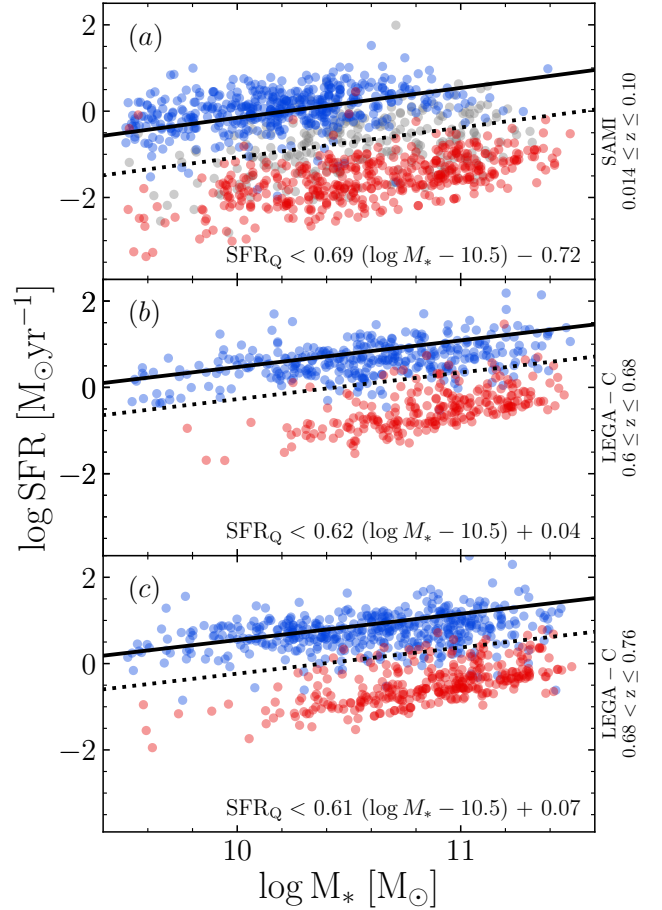


**Figure 1.** Star formation rate versus stellar mass for the three redshift bins. The black solid lines are the redshift-dependent main sequence from Whitaker et al. (2012, see Equation 1). The dotted black lines are the adopted boundary between quiescent and star-forming galaxies, defined as  $\text{SFR}_Q < \text{SFR}_{MS} - 2\text{RMS}$  (bottom right of each panel), where RMS is the measured scatter about the main sequence based on an initial cut 1 dex below the relation. The points are coloured using quiescent (red points), star-forming (blue points), and intermediate (grey points; panel a only) selection criteria from the literature (see Section 2.3); our adopted selection criteria are comparable to these alternatives.

sample was selected, the Driver et al. (2018) catalogue also includes measurements for the G10-COSMOS region (Davies et al. 2015; Andrews et al. 2017) which includes 301 LEGA-C galaxies. We use this overlap of 301 galaxies to check for systematic biases between the samples that might arise from the different photometric bands used in the SED fits. We find good agreement between the two catalogues for both the stellar masses and the star formation rates. The mean difference between the two catalogues is  $0.08 \pm 0.15\text{dex } \log M_*$  and  $0.07 \pm 0.40\text{dex } \log \text{SFR}$ , with the values from de Graaff et al. (2021) being slightly more massive and more highly star-forming.

We separate quiescent and star-forming galaxies in both the LEGA-C and SAMI samples based on distance from the redshift-dependent star-forming main sequence defined by Whitaker et al. (2012):

$$\log \text{SFR} = (0.70 - 0.13z)(\log M_* - 10.5) + 0.38 + 1.14z - 0.19z^2 \quad (1)$$

We show this relation in Figure 1 (solid black line) using the central redshift value in each bin ( $z = 0.057, 0.64, 0.72$ ). We do an initial cut 1 dex below the relation and measure the root-mean-square

<sup>2</sup> The data can be accessed at <https://docs.datacentral.org.au/sami/>



(RMS) scatter about the trend. We then define quiescent galaxies as those with  $\text{SFR}_Q < \text{SFR}_{MS} - 2\text{RMS}$  (dotted black line). The precise selection cut for each redshift bin is given in each panel of Figure 1.

We use the star-forming main sequence as defined by Whitaker et al. (2012), because their analysis used the same cosmological parameters and IMF assumed in this work, and cover the full redshift range of both the LEGA-C and SAMI samples. We note however that the Whitaker et al. (2012) results are based on linear fits in the  $\log \text{SFR} - \log M_*$  plane, but more recent works have shown that the star-forming main sequence turns over at high stellar masses (e.g. Leslie et al. 2020). We therefore test our analysis using other quiescent selection criteria used in the literature for the two surveys, and find our results are insensitive to reasonable changes to the quiescent sample selection.

In Figure 1 we compare our quiescent selection criterion to others used in the literature for the two surveys. The SAMI galaxies (panel a) are coloured by the selection used in Croom et al. (2021b), which is based on the star formation rates from Medling et al. (2018) and distance from the Renzini & Peng (2015) main sequence. The LEGA-C galaxies (panels b and c) are coloured by their U–V vs V–J diagram classification (Labbé et al. 2005), as defined by Muzzin et al. (2013b) and used in, e.g., Chauke et al. (2018), Wu et al. (2018) and Straatman et al. (2018). Figure 1 shows that our quiescent selection based on distance from the Whitaker et al. (2012) main sequence is comparable to these alternative selection criteria used in the literature and our results are unchanged if we instead adopt these alternate quiescent selection criteria. We use the quiescent criteria based on the Whitaker et al. (2012) main sequence and MAGPHYS derived SFR and  $M_*$  for consistency across the two surveys.

Post-starburst galaxies are a subclass of quiescent galaxies that recently quenched after a burst of star-formation (Dressler & Gunn 1983; Balogh et al. 1999; Dressler et al. 1999), and therefore contain a young average stellar population. As a result of their rapid quenching (Wu et al. 2020), post-starburst galaxies tend to be smaller than the rest of the quiescent population at fixed mass (Whitaker et al. 2012; Yano et al. 2016; Almaini et al. 2017). The young average ages and small sizes of post-starburst galaxies are contrary to the rest of the quiescent population in which young galaxies tend to be larger at fixed mass (Wu et al. 2018). We test our analysis on a sample without post-starburst galaxies (defined as quiescent galaxies with an equivalent width of  $H_\delta > 4\text{\AA}$ ; e.g. Wu et al. 2018; D’Eugenio et al. 2020). Our results are qualitatively unchanged if we exclude post-starburst galaxies. We therefore we include post-starburst galaxies in our quiescent sample.

We compare the data quality between the two surveys by comparing the median spectral S/N per  $\text{\AA}$  in the rest-wavelength range covered by all targets (4427–4548  $\text{\AA}$ ), with  $K_s$ -band photometry from VISTA (Visible and Infrared Survey Telescope for Astronomy; Sutherland et al. 2015). SAMI galaxies have  $K_s$  magnitudes measured as part of the VISTA Kilo-Degree Infrared Galaxy survey (VIKING; Edge et al. 2013), while the LEGA-C targets are selected from the UltraVISTA survey (McCracken et al. 2012). In Figure 2 we compare the apparent  $K_s$  magnitude to the median S/N per  $\text{\AA}$  measured from the full-spectral fits for the quiescent samples (see Section 3). Figure 2 shows that despite the fainter apparent magnitudes of the LEGA-C targets, the longer integration time ( $\sim 20$  hours compared to  $\sim 3.5$  hours for SAMI) and larger mirror diameter (8 m vs 4 m) leads to a sample with a comparable S/N range to the low-redshift SAMI sample.

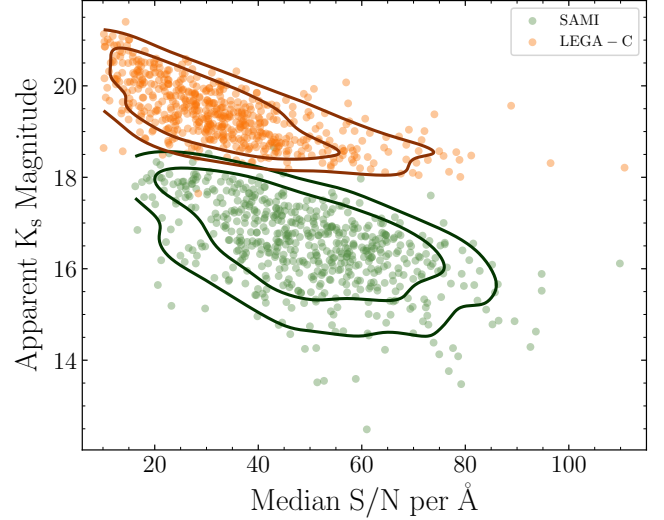


**Figure 2.** Apparent  $K_s$  magnitude versus the median spectral S/N per  $\text{\AA}$  in the rest-wavelength region 4427–4548  $\text{\AA}$  for SAMI (green) and LEGA-C (orange) quiescent galaxies. Despite the different redshift ranges and apparent magnitudes of the targets, the significantly longer integration time of the LEGA-C survey leads to a sample with a range in S/N per  $\text{\AA}$  comparable to the SAMI sample.

#### 2.4 Redshift dependence across the mass–size plane

It is well established that both the star-forming and quiescent populations evolve in the mass–size plane with redshift (e.g. van der Wel et al. 2014; Hill et al. 2017; Faisst et al. 2017; Mowla et al. 2019). Given we are interested in analysing how stellar age and metallicity vary in the mass–size plane between our samples at different redshifts, we first want to ensure the size evolution within each sample is negligible. Both van der Wel et al. (2014) and Mowla et al. (2019) analysed the distribution of quiescent and star-forming galaxies in the mass–size plane in redshift bins of width 0.5 over the range  $0 \leq z \leq 3$  and parameterised the evolution in the median size of star-forming and quiescent galaxies as:

$$r_{\text{eff}} [\text{kpc}] = B_z \times (1 + z)^{-\beta_z} \quad (2)$$

For intermediate mass galaxies ( $\log M_*/M_\odot \sim 10.75$ ), van der Wel et al. (2014) found  $\beta_z = 1.24 \pm 0.08$  for quiescent galaxies and  $\beta_z = 0.72 \pm 0.09$  for star-forming galaxies. For massive galaxies ( $\log M_*/M_\odot > 11.3$ ), Mowla et al. (2019) found  $\beta_z = 1.40 \pm 0.07$  and  $1.09 \pm 0.15$  for quiescent and star-forming galaxies respectively.

Using these relations, we can estimate the median size evolution for both intermediate and high mass galaxies within each redshift bin. Table 1 summarises these results, expressed as  $\log R_e(z_{\min}) - \log R_e(z_{\max})$  where  $z_{\min}$  and  $z_{\max}$  are the minimum and maximum redshift values in each bin. We want to ensure that any possible evolution in the median size of the population over the redshift range of each bin is less than the median uncertainty on the effective radii, while also maximising the sample size within each bin. For both the SAMI and LEGA-C samples,  $\sigma_{\log R_e} = 0.05$  dex. We therefore want the fewest number of redshift bins such that  $\log R_e(z_{\min}) - \log R_e(z_{\max}) < 0.05$  dex.

For the full SAMI redshift range ( $0.004 \leq z \leq 0.11$ ), both the intermediate and high mass quiescent populations have size growth greater than  $\log R_e(z_{\min}) - \log R_e(z_{\max}) > 0.05$  dex (0.054 for intermediate mass and 0.060 for high mass); we therefore require a

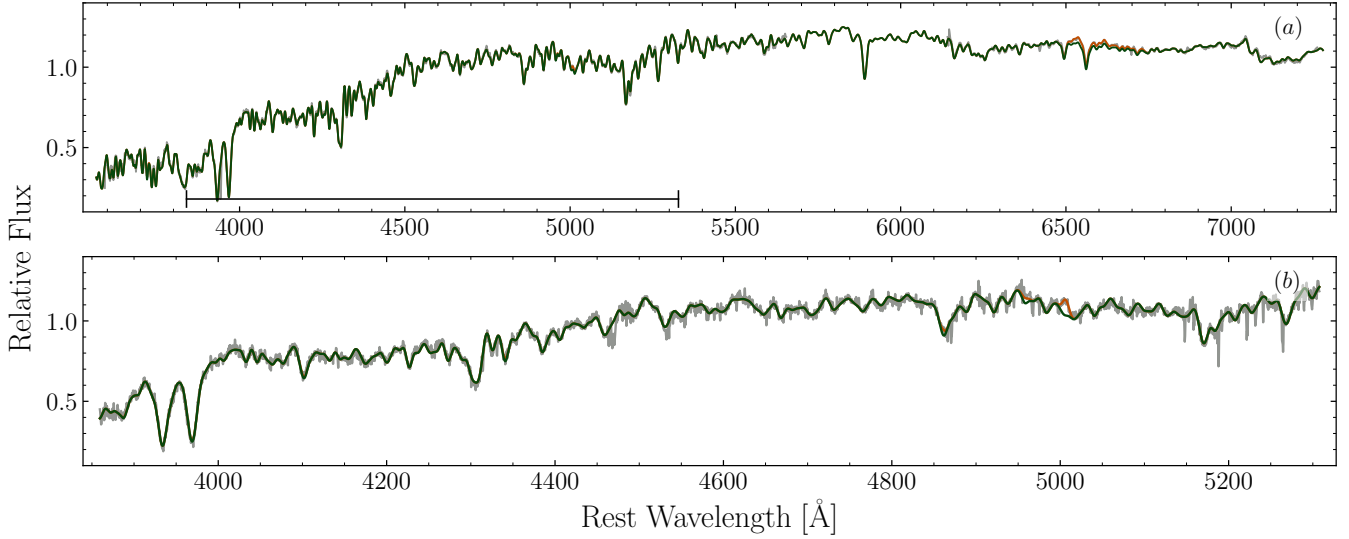


**Figure 3.** Example full spectral fits for SAMI galaxy ID=278109 (panel a) and LEGA-C galaxy ID=206573, mask ID=1 (panel b). In both panels the original spectrum is shown in grey, with the best-fit from the stellar templates in green and the best-fit emission templates in orange. By simultaneously fitting the stellar and gas components, we are able to recover absorption features masked by emission lines. The black horizontal line in panel a shows the wavelength range of panel b for ease of comparison. The fluxes are normalised such that the median flux across the spectrum is 1.

$z_{\min}$	$z_{\max}$	Intermediate Mass		High Mass	
		Quiescent	Star-Forming	Quiescent	Star-Forming
		$\log R_e(z_{\min}) - \log R_e(z_{\max})$ [dex]			
0.014	0.100	0.044	0.025	0.049	0.039
0.600	0.680	0.026	0.015	0.030	0.023
0.680	0.760	0.025	0.015	0.028	0.022
0.004	0.110	0.054	0.031	0.061	0.048
0.600	0.760	0.051	0.030	0.058	0.045

**Table 1.** Evolution in the median size across each redshift bin expressed as  $\log R_e(z_{\min}) - \log R_e(z_{\max})$  based on the size–redshift relations of [van der Wel et al. \(2014\)](#) and [Mowla et al. \(2019\)](#).

narrower redshift range. We remove 22 galaxies at the ends of the redshift range to leave a sample spanning  $0.014 \leq z \leq 0.10$ , so that the size evolution is now less than 0.05 dex.

The size evolution with redshift of the LEGA-C  $0.60 \leq z \leq 0.76$  sample is shown in the bottom row of Table 1. Across this redshift range, both the intermediate and high mass quiescent populations have size growth greater than  $\log R_e(z_{\min}) - \log R_e(z_{\max}) > 0.05$  (0.051 for intermediate mass and 0.058 for high mass); we therefore require narrower redshift bins. If we split the LEGA-C sample into two redshift bins of width  $\Delta z = 0.08$ , namely  $0.60 \leq z \leq 0.68$  and  $0.68 < z \leq 0.76$ , we see from Table 1 that the size evolution within these bins is now less than 0.05 dex. This width of  $\Delta z_{\text{LEGA-C}} = 0.08$  has the additional advantage of being comparable to the SAMI redshift range of  $\Delta z_{\text{SAMI}} = 0.086$  and so there is similar median size evolution within all three bins. We therefore split the LEGA-C sample into these two redshift bins,  $0.60 \leq z \leq 0.68$  and  $0.68 < z \leq 0.76$ , with 550 (241 quiescent, 309 star-forming) and 684 (312 quiescent, 372 star-forming) galaxies respectively.

### 3 STELLAR POPULATION MEASUREMENTS

Luminosity-weighted stellar population parameters for both the LEGA-C and SAMI galaxies are measured from full spectral fits using 350 theoretical templates based on the Extended Medium resolution INT Library of Empirical Spectra (E-MILES; [Sánchez-Blázquez et al. 2006](#); [Vazdekis et al. 2010](#)), isochrones from [Girardi et al. \(2000\)](#) and a [Chabrier \(2003\)](#) initial mass function. The templates range in age from 0.063 to 17.78 Gyr, and range in  $[Z/H]$  from  $-2.32$  to  $+0.22$ , and have  $[\alpha/Fe]$  values scaled to the solar neighbourhood (the "base" models; [Vazdekis et al. 2010](#)). We test our analysis using the BaSTI isochrones ([Pietrinferni et al. 2004, 2006](#)) and found our results qualitatively unchanged. We fit the templates to the deredshifted spectra using the Python implementation of the publicly available Penalized Pixel-Fitting software (pPXF; [Cappellari & Emsellem 2004](#); [Cappellari 2017](#)). We do an initial fit to ensure that we have a good estimate of the S/N ratio per pixel and multiply the noise by a rescaling coefficient so that the reduced  $\chi^2$  is unity. The median rescaling is 1.45 for the LEGA-C sample and 0.54 for the SAMI sample, with standard deviations of 0.31 and 0.21 respectively. We then use this improved estimate of the noise for the second (final) fit. To account for dust reddening and any offsets to the continuum shape due to flux calibration, this final fit includes a 10<sup>th</sup> degree multiplicative polynomial.

The final age and metallicity values are the weighted average of all the templates:

$$\log \text{Age} = \frac{\sum w_i \log \text{Age}_i}{\sum w_i} \quad (3)$$

$$[Z/H] = \frac{\sum w_i [Z/H]_i}{\sum w_i} \quad (4)$$

where  $w_i$  is the weight measured from pPXF for the  $i^{\text{th}}$  template, with single-burst age and metallicity values and  $[Z/H]_i$  and  $\text{age}_i$ . Following [McDermid et al. \(2015\)](#), the weighted average age is mea-

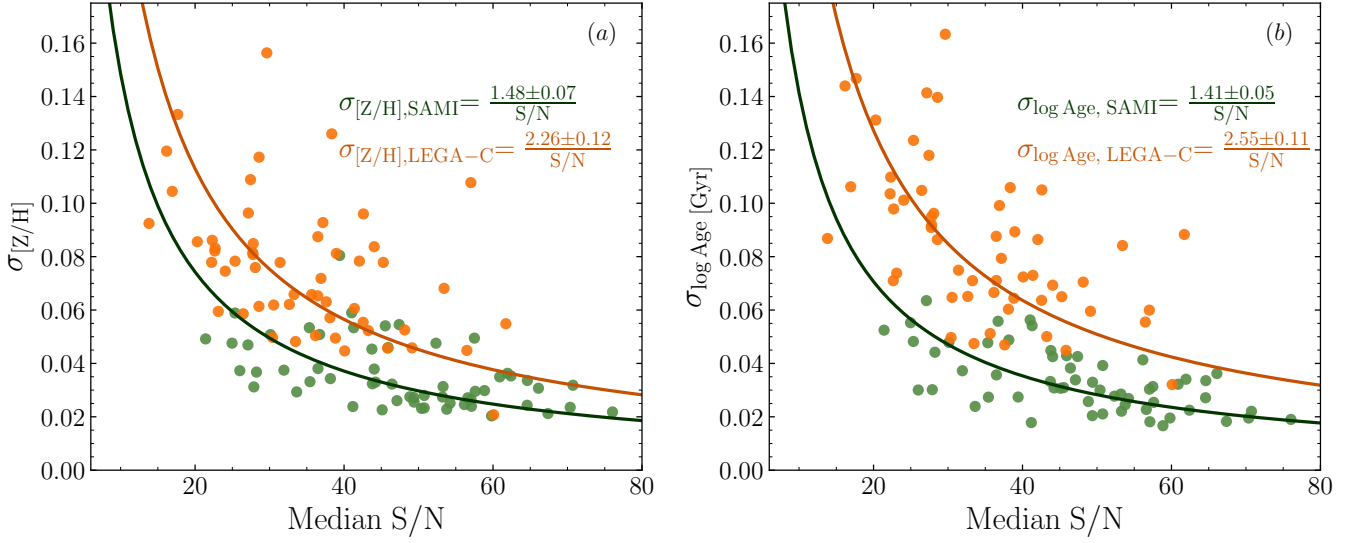


**Figure 4.** Uncertainty on luminosity-weighted [Z/H] (panel a) and age (panel b) versus the median S/N per Å of the spectrum in the rest wavelength range 4427–4548 Å for a sample of 56 LEGA-C (orange points) and 58 SAMI (green points) quiescent galaxies. The coloured lines are the best-fit inverse relations (top right of each panel), which are used to assign uncertainties to [Z/H] and age for all galaxies in the samples based on their spectral S/N.

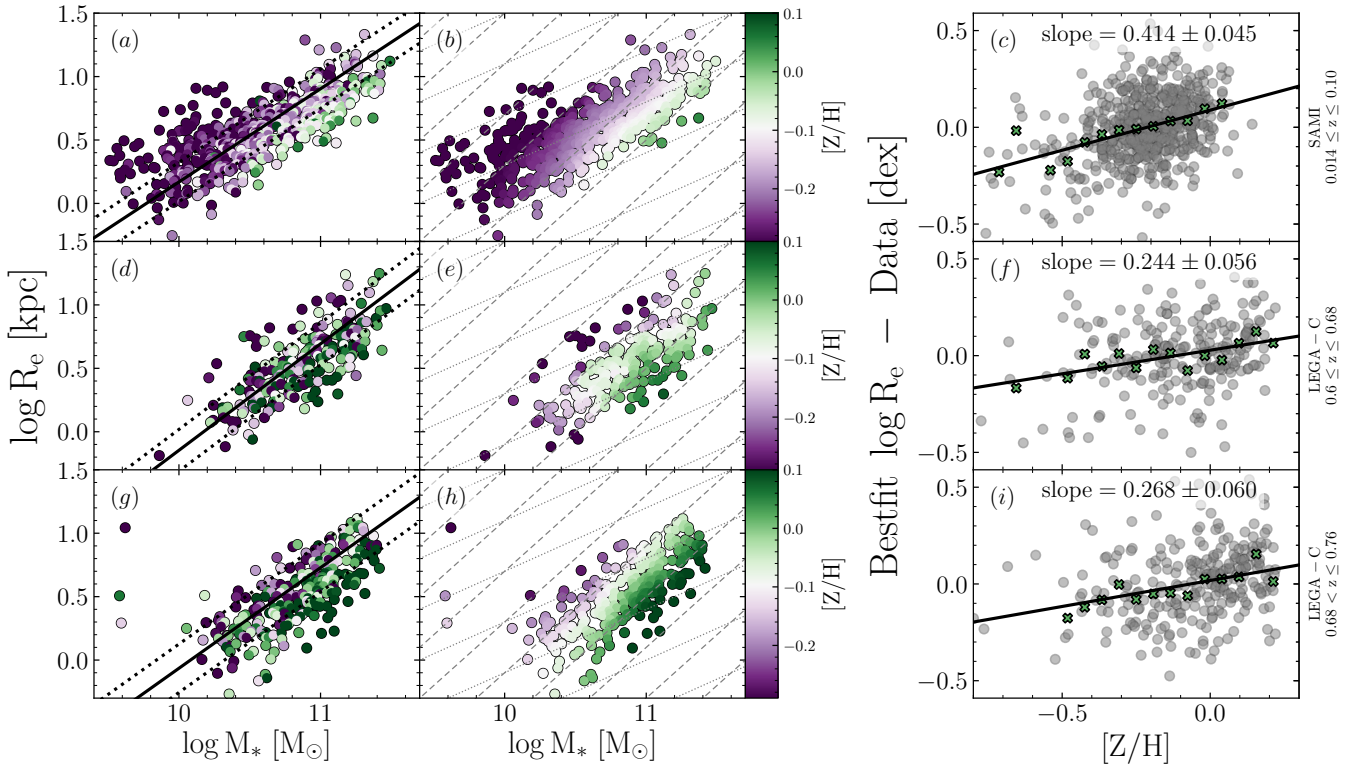


**Figure 5.** Stellar metallicity [Z/H] of quiescent galaxies in the mass–size plane for three redshift bins. The top row shows the SAMI galaxies  $0.014 \leq z \leq 0.10$ , middle row the LEGA-C galaxies with  $0.60 \leq z \leq 0.68$ , and the bottom row the LEGA-C galaxies with  $0.68 < z \leq 0.76$ . The colour scale of the left column represents metallicity and the centre column shows the smoothed metallicity using the LOESS algorithm. The best-fits are shown in the left column (black solid line) with the fitted  $1\sigma$  intrinsic scatter (black dotted lines). In the centre column, the dashed lines show constant surface density  $\Sigma \propto M_*/R_e^2$ . The right column shows the dependence of the residuals (model - data) from the best-fit mass–size relation with metallicity. The black line in the right column is the best-fit relation to the residuals, with the slope written at the top of each panel. The crosses show the median value in independent bins with 3 or more galaxies. This Figure suggests that metallicity varies with  $M_*/R_e$  (dashed lines in the middle column) in all three redshift bins.

sured using the logarithm of the template ages because the template ages are sampled logarithmically.

All fits are done without linear regularisation, which imposes constraints on the weights of neighbouring templates (in age-metallicity space) to vary smoothly. While using linear regularisation produces more realistic star-formation histories, reasonable degrees of regularisation do not significantly change the weighted average age and  $[Z/H]$  values (B20).

In addition to the stellar templates, we also include templates for common gas emission lines. We fix the flux ratios of the Balmer series from  $H_\alpha$  to  $H_\theta$  assuming a decrement based on Case B recombination (electron temperature  $T = 10^4$  K and number density  $n = 100 \text{ cm}^{-3}$ ; Dopita & Sutherland 2003), using the TIE\_BALMER pPXF keyword. Any residual difference in flux from the fixed ratios is attributed to dust extinction, which is fit using a Calzetti et al. (2000) extinction curve (via the GAS\_REDDENING keyword). We also limit the ratios of the [OII] and [SII] doublets to lie within the theoretical ranges predicted by atomic physics (Osterbrock & Ferland 2006) using the LIMIT\_DOUBLETs keyword. The [OIII], [OI] and [NII] doublets also each have their flux ratios tied based on atomic physics. We show example fits in Figure 3 for SAMI galaxy ID=278109 and LEGA-C galaxy ID=206573 mask ID=1.

We tested the resulting age and metallicity values from fits to SAMI spectra (typical rest wavelength range  $\sim 3461\text{--}7077 \text{ \AA}$ ) that were restricted to use the rest wavelength range typical of the LEGA-C sample ( $\sim 3723\text{--}5168 \text{ \AA}$ ). We found good agreement for both the age and metallicity values, however the age values in the reduced wavelength range were on average  $0.067 \pm 0.064$  dex younger than when fitted using the full SAMI wavelength range. Given we are interested in the age variations *within* each redshift bin, our results and interpretations are not affected by this minor discrepancy.

We estimate uncertainties for the age and metallicity measurements for both the LEGA-C and SAMI samples. Due to the computational expense, we explicitly test 10% of quiescent galaxies randomly selected from each survey (56 and 58 for the LEGA-C and SAMI samples respectively) and fit the measured uncertainties as a function of the median S/N per  $\text{\AA}$ . We then apply this S/N-dependent uncertainty value to the rest of each sample. We estimate the S/N per  $\text{\AA}$  based on the scaled variance from the initial pPXF fit and take the median S/N in the rest wavelength range  $4427\text{--}4548 \text{ \AA}$ . This wavelength range was chosen because it is covered by all galaxies in the two samples.

For the tested galaxies, we shuffle the residuals from the best-fit within wavelength bins approximately  $500 \text{ \AA}$  wide; these shuffled residuals are then added to the best-fit spectrum and refit. This process is repeated 100 times per galaxy, building up a distribution of values in age and metallicity. The distributions are approximately Gaussian and centred around the original fit value, so we take the standard deviations of the distributions as the uncertainties on the original age and metallicity measurements. Figure 4 shows the measured uncertainty and the median spectral S/N for the tested galaxies. We fit the dependence between the measured uncertainties and the S/N as an inverse relation using the Levenberg-Marquardt least-squares optimisation algorithm in Python using the SciPy package's OPTIMIZE\_CURVE\_FIT routine (Virtanen et al. 2020). These relations,  $\sigma_{[Z/H]} = \frac{2.26 \pm 0.12}{S/N}$  and  $\sigma_{\log \text{Age}} = \frac{2.55 \pm 0.11}{S/N}$  for LEGA-C and  $\sigma_{[Z/H]} = \frac{1.48 \pm 0.07}{S/N}$ , and  $\sigma_{\log \text{Age}} = \frac{1.41 \pm 0.05}{S/N}$  for SAMI, are then used to assign uncertainties to the age and metallicity of the rest of the galaxies in each sample based on their S/N.

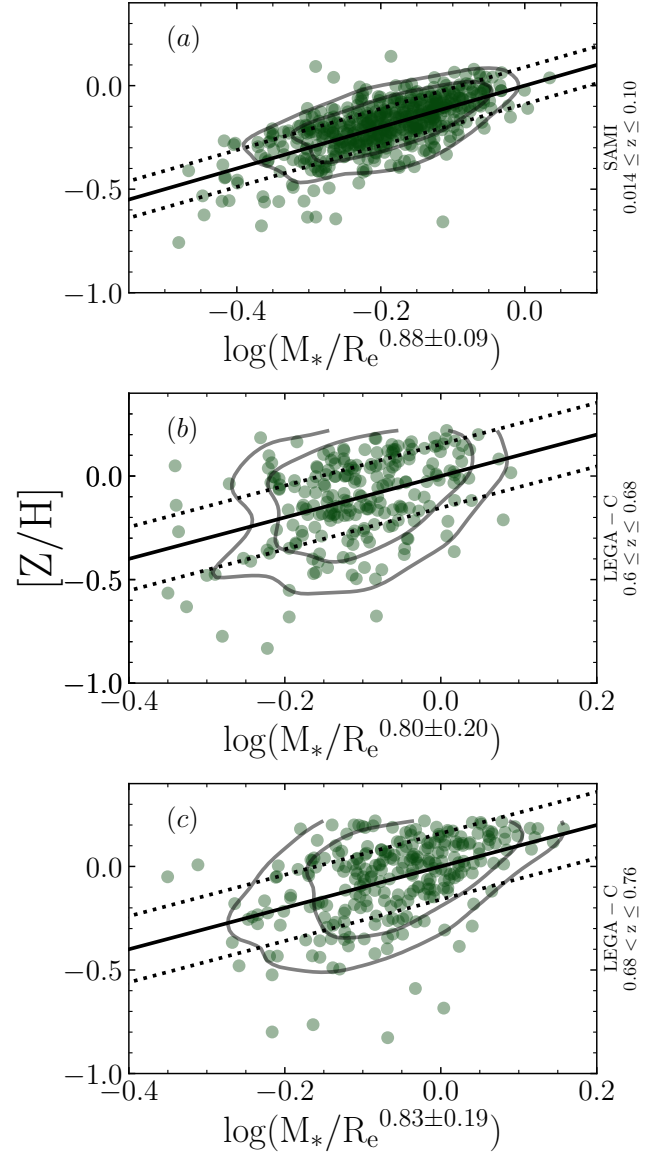


**Figure 6.** Stellar metallicity  $[Z/H]$  versus the best-fit linear combination of  $M_*$  and  $R_e$  for the three redshift bins. The top panel (a) shows the SAMI galaxies  $0.014 \leq z \leq 0.10$ , the middle panel (b) shows the LEGA-C galaxies with  $0.60 \leq z \leq 0.68$ , and the bottom panel (c) the LEGA-C galaxies with  $0.68 < z \leq 0.76$ . The best-fit ratio of coefficients between  $\log M_*$  and  $\log R_e$  is statistically consistent within  $\sim 2\sigma$  across all three redshift bins and with a ratio of  $-1$ .

## 4 RESULTS

All linear fits are done using a Bayesian approach with uniform priors on the angle of the line and the intercept and a Jeffreys (1946) prior on the intrinsic scatter in the y-direction. First we find the mode of the posterior function using the differential evolution numerical method (Storn & Price 1997). This is followed by Markov Chain Monte Carlo integration of the posterior distribution to estimate the uncertainties on the model parameters, using the Python package EMCEE (Foreman-Mackey et al. 2013), which implements the affine-invariant ensemble sampler of Goodman & Weare (2010). A similar Bayesian approach is used for the plane fits in Section 4.1, with uniform priors on the slopes



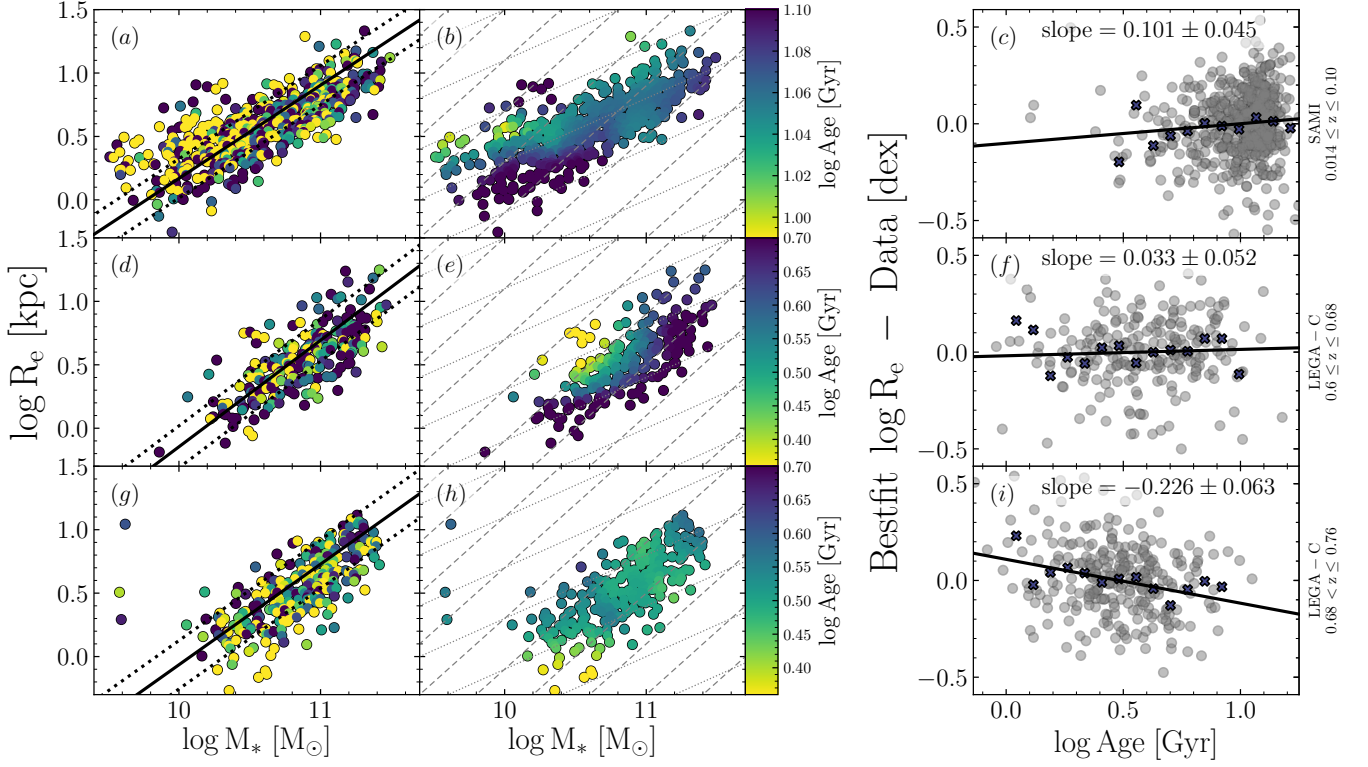


**Figure 7.** Stellar age in the mass–size plane for quiescent galaxies in the three redshift bins. The top row shows the SAMI data with  $0.014 \leq z \leq 0.10$ , middle row the LEGA-C data with  $0.60 \leq z \leq 0.68$ , and the bottom row the LEGA-C data with  $0.68 < z \leq 0.76$ . The colour scale of the left column represents the stellar age, and the centre column shows the smoothed age using the LOESS algorithm. The best-fits are shown in the left column (black solid line) with the fitted  $1\sigma$  intrinsic scatter (black dotted lines). In the centre column the dashed lines show constant  $M_*/R_e$  and the dotted lines show constant surface mass density  $\Sigma \propto M_*/R_e^2$ . The right column shows the dependence of the residuals (model - data) from the best-fit mass–size relation with age. The black line in the right column is the best-fit relation to the residuals, with the slope written at the top of each panel. The crosses show the median value in independent bins with 3 or more galaxies. This Figure illustrates that variations in age in the mass–size plane change with redshift.

and intercepts and a [Jeffreys \(1946\)](#) prior on the intrinsic scatter in the y-direction (i.e. in the stellar population parameter). For illustrative purposes we emphasise the presence/absence of residual trends by smoothing the colour distributions using the LOESS locally weighted regression algorithm ([Cleveland & Devlin 1988](#); [Cappellari et al. 2013a](#)), however all fits are done on the unsmoothed data. The LOESS algorithm takes into account the uncertainty on the stellar population parameter (age or metallicity), therefore highly uncertain points may have a significantly different value in the LOESS smoothed colour map compared to the unsmoothed data.

#### 4.1 Metallicity [Z/H]

We start by showing how luminosity-weighted [Z/H] varies in the mass–size plane, and quantify this variation by analysing how the residuals from the best-fit mass–size relation (residuals = model - data) trend with [Z/H] (Figure 5). In all three redshift bins (rows) of Figure 5 we see significant dependence of metallicity on both mass and size. The LOESS-smoothed distributions (middle column) highlight that [Z/H] varies essentially along lines of constant  $M_*/R_e$ . Furthermore, the residual trends are qualitatively the same, in that galaxies below the mass–size relation (smaller at fixed mass) tend to have higher metallicities in all three redshift bins.

The dependence of [Z/H] on both mass and size is further quantified in Figure 6, which shows [Z/H] fit as a linear combination

of  $\log M_*$  and  $\log R_e$ ,  $[Z/H] = a \log M_* + b \log R_e + c$ . The ratio of the coefficients of  $\log M_*$  and  $\log R_e$  in the best-fit relations are  $a/b = -0.88 \pm 0.09, -0.80 \pm 0.20, -0.83 \pm 0.19$  for  $z \in [0.014, 0.10]$ ,  $z \in [0.60, 0.68]$ , and  $z \in [0.68, 0.76]$  respectively. All three ratios are within  $\sim 2\sigma$  uncertainty of  $-1$ , the ratio representing the gravitational potential ( $\Phi \propto M_*/R_e$ ). Furthermore these ratios are significantly different from 0 (the ratio representing scaling solely with  $M_*$ ) and 2 (scaling with surface density  $\Sigma \propto M_*/R_e^2$ ).

#### 4.2 Age

We show how luminosity-weighted age varies in the mass–size plane and quantify how the residuals from the best-fit mass–size relation (residuals = model - data) vary with age in Figure 7. Our results show that stellar age scales with mass and size differently across redshift. For a clear visual representation of the results, we can compare the smoothed colour scale in the middle column from the highest to the lowest redshift bin (middle column, bottom to top row of Figure 7). The age dependence goes from trending *along* the mass–size relation (panel h), to no obvious dependence (panel e), to there being a strong dependence perpendicular to the relation (panel b). This variation is also apparent in the unsmoothed data (left column) and is quantified in the changing trend between age and residuals from the best-fit (right column). In the highest redshift bin (panel i), at fixed mass there is a mild negative trend with age in that smaller galaxies are on

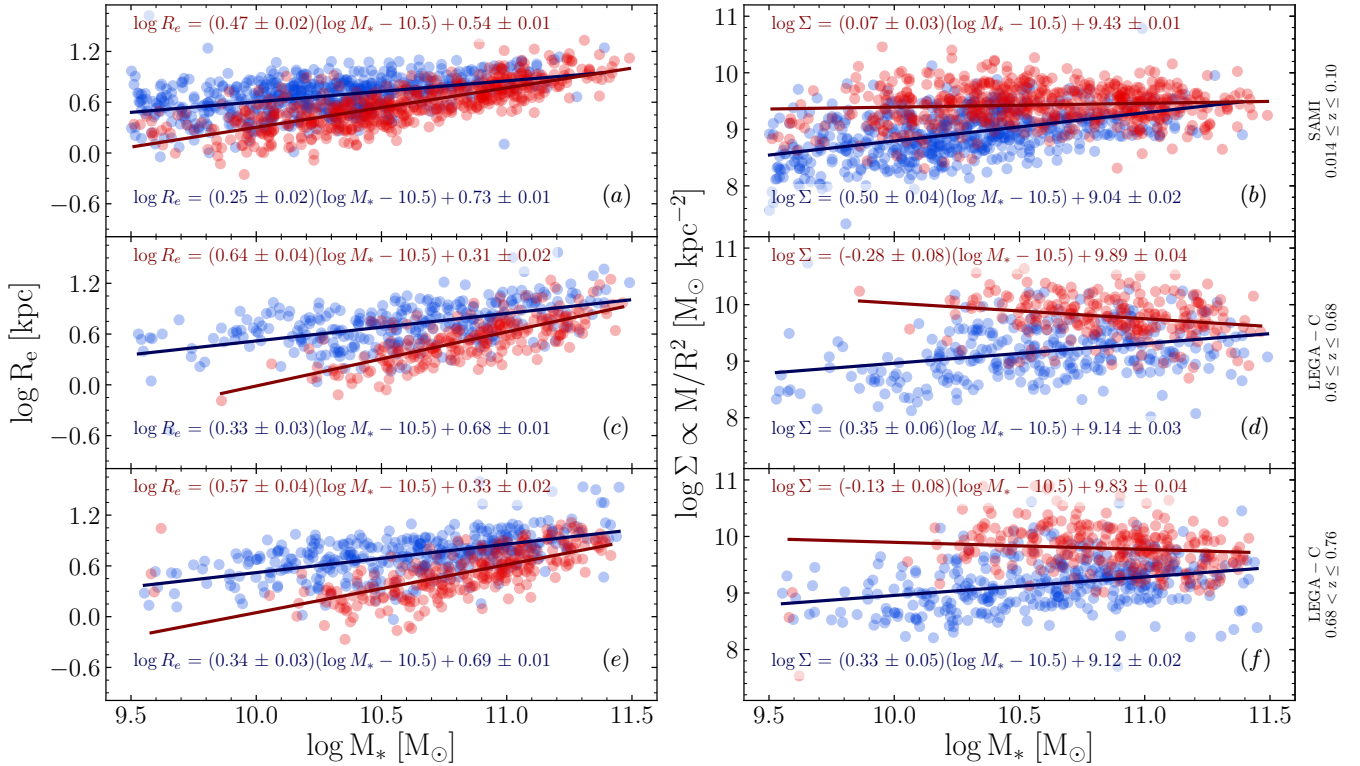


**Figure 8.** Mass–size (left column) and mass–surface density (right column) relations for the three redshifts bins. The top row shows the SAMI data with  $0.014 \leq z \leq 0.10$ , middle row the LEGA-C data with  $0.60 \leq z \leq 0.68$ , and the bottom row the LEGA-C data with  $0.68 < z \leq 0.76$ . The red points are quiescent galaxies and the blue points are star-forming galaxies. The solid red and blue lines are the best-fit relations to the quiescent and star-forming populations respectively. In each panel we show the equation of the best-fit relation (in red at top for quiescent galaxies and in blue at bottom for star-forming galaxies).

average younger. In contrast, in the intermediate redshift bin there is no statistically significant residual trend (panel f). Finally (panel c), in the lowest redshift bin, there is a mild trend for smaller galaxies at fixed mass to be older. The change in the correlation between age and  $\Sigma$  with redshift suggests the relation observed at  $z \sim 0$  is built up over time and that at least one of the processes driving the evolution of stellar mass, size and/or star formation history has a redshift dependence.

We note in particular that in the  $z \sim 0$  mass–size plane age trends along lines of constant  $\Sigma \propto M/R^2$  (i.e. lines with slope = 0.5), remarkably similar to the slope of the quiescent population itself in the mass–size plane. This result is evident from the unsmoothed data (panel a), but clearest in the LOESS-smoothed data in panel b of Figure 7 which shows that the LOESS-smoothed age varies perpendicularly to the mass–size relation. In the next section we investigate how the  $z \sim 0$  age– $\Sigma$  relation relates to the slope of the quiescent population in the mass–size plane and show how it results from the build-up of the quiescent population over time.

### 4.3 Population evolution in the mass–size plane

It is well established that the median size of galaxies in both the quiescent and star-forming populations evolves significantly in the mass–size plane with redshift (Ferguson et al. 2004; Trujillo et al. 2007; Buitrago et al. 2008; Williams et al. 2010). Specifically, van der Wel et al. (2014) and Mowla et al. (2019) showed that for  $0 \leq z \leq 3$ , the slopes of the mass–size relations for both the quiescent and star-forming populations change little with redshift, but the intercepts

decrease with increasing redshift such that high-redshift populations are smaller at fixed mass.

We reproduce these results in the left column of Figure 8, which shows the quiescent and star-forming populations in the mass–size plane for each redshift bin. Based on previous studies we expect the intercepts to decrease with increasing redshift. There is a clear decrease in the intercept from the lowest to highest redshift bin, but the intercepts of the two LEGA-C bins are the same within the uncertainty. However, from Mowla et al. (2019) the change in the intercept in this redshift range for the star-forming and quiescent sequences are  $\Delta_{SF} = -0.006$  dex and  $\Delta_Q = -0.01$  dex respectively, for which our results are consistent within the uncertainties.

In agreement with these previous studies we find the slopes stay relatively constant. Crucially, and in agreement with Mowla et al. (2019), the slopes of the quiescent populations in the mass–size plane are approximately proportional to  $\log R_e \approx 0.5 \log M_*$  (specifically,  $0.47 \pm 0.02$ ,  $0.64 \pm 0.04$  and  $0.57 \pm 0.04$  for  $z \in [0.014, 0.10]$ ,  $z \in [0.60, 0.68]$  and  $z \in [0.68, 0.76]$  respectively). This slope of  $\sim 0.5$  in the mass–size plane means that, at fixed redshift, the quiescent population has an approximately constant surface–mass density regardless of stellar mass. For some redshift-dependent constant  $k_1(z)$ ,

$$\log R_e = 0.5 \log M_* + k_1(z) \quad (5)$$

$$\log \Sigma = \log M_* - 2 \log R_e = -2k_1(z) \quad (6)$$

which implies that surface density does not change with stellar mass:

$$\frac{\delta \log \Sigma}{\delta \log M_*} = 0 \quad (7)$$

Indeed, in the right column of Figure 8 we show the mass–surface density plane and find that the slopes of the quiescent populations are all close to zero (within  $2\sigma$  for panel f,  $3\sigma$  for panel b, and within  $4\sigma$  for panel d). Furthermore, as expected, the intercepts in the mass–surface density plane increase with increasing redshift, such that the LEGA-C quiescent galaxies are more compact (higher  $\Sigma$ ) than the lower redshift SAMI quiescent galaxies.

The individual evolutionary tracks of star-forming galaxies are expected to closely align with the star-forming population in the mass–size plane, a result supported by both observations and simulations (Lilly et al. 1998; Ravindranath et al. 2004; Trujillo et al. 2006b; van Dokkum et al. 2015). Therefore the slope of  $\sim 0.3$  for the star-forming sequence in the mass–size plane in all three redshift bins means that as galaxies build up their mass via in-situ star formation, they also increase their surface density. For some redshift-dependent constant  $k_2(z)$ ,

$$\log R_e = 0.3 \log M_* + k_2(z) \quad (8)$$

$$\log \Sigma = \log M_* - 2 \log R_e = 0.4 \log M_* - 2k_2(z) \quad (9)$$

which implies surface density increases with increasing stellar mass:

$$\frac{\delta \log \Sigma}{\delta \log M_*} = 0.4 \quad (10)$$

Combining these two key results suggests that star-forming galaxies build their stellar mass, and at the same time increase their stellar surface density until they reach a redshift-dependent threshold surface density at which they quench. As this threshold surface density decreases with decreasing redshift, the quiescent population is built up to include galaxies that have quenched at a range of redshifts and, consequently, with a range of surface densities. In the  $z \sim 0$  quiescent population, therefore, a galaxy’s surface density reflects the redshift at which it quenched (luminosity-weighted age is closely tied to how long ago the galaxy quenched).

This connection between quenching and galaxy structure, in particular surface density, is in agreement with previous work. Franx et al. (2008) found a redshift-dependent threshold surface density above which galaxies have low sSFR (are quiescent) and below which the sSFR are high with little variation (are star-forming). Franx et al. (2008) also found that the surface density threshold increases with increasing redshift. Similarly, van der Wel et al. (2009) found that stellar velocity dispersion also shows a redshift-dependent threshold separating quiescent and star-forming galaxies. Additionally, González Delgado et al. (2014a) found a threshold surface-mass density for low-redshift spheroidal galaxies that is nearly independent of stellar mass, in agreement with our results.

Recent work by Chen et al. (2020) provides a theoretical framework explaining the relation between surface density and quenching. Chen et al. (2020) showed that a galaxy model in which central black hole mass (and therefore strength of AGN feedback) is related to both the host galaxy’s mass and size successfully explains key properties of star-forming and quenched galaxies. In the model larger star-forming galaxies at fixed mass have smaller central super-massive black holes (due to their lower central surface density). Therefore these extended galaxies evolve to higher stellar masses before the central AGN has strong enough feedback to shock-heat infalling gas from the halo, quenching star formation.

Clearly, this scenario of a redshift-dependent quenching surface-density requires that passive evolution does not significantly alter

the inner structure of quiescent galaxies (inside  $\sim 1 R_e$ ); however, we note that if this assumption was incorrect, it would be even harder to explain the observed correlation between stellar-population age and surface mass density. We discuss the effect of passive evolution in Section 5.3.

## 5 DISCUSSION

Our aim was to investigate how scaling relations between galaxy structure and global stellar metallicity and age change across  $\sim 6$  Gyr, to understand the redshift dependence in stellar population evolution. We aimed to test two hypotheses:

(i) The  $[Z/H]-M_*/R_e$  relation is consistent with the gravitational potential regulating the retention of stellar and supernova ejecta via its relation to the escape velocity; if this is true, there should be a relation at every redshift.

(ii) The  $z \sim 0$  age– $\Sigma$  relation is built up over time due to galaxies forming and evolving more compactly (diffusely) at higher (lower) redshifts; in this case, the age– $\Sigma$  relation should be less prominent at intermediate redshifts than at  $z \sim 0$ .

Our results support both these hypotheses: (i) The metallicity of intermediate-redshift quiescent galaxies, like that of low-redshift quiescent (B18) and star-forming galaxies (B20), is strongly correlated with  $M_*/R_e$  (Section 4.1); we discuss this further in Section 5.1. (ii) At intermediate redshifts, there is no statistically significant correlation between global stellar age and surface mass density (Section 4.2); we show how the  $z \sim 0$  age– $\Sigma$  could result from the redshift-evolution of the mass–size plane (Section 4.3) and further discuss this hypothesis in Section 5.2.

### 5.1 The consistency of the $[Z/H]-\Phi$ relation across 6 Gyr

We find that from low to intermediate redshift ( $z \leq 0.76$ ) the stellar metallicity of quiescent galaxies correlates more tightly with  $M_*/R_e$  than with other combinations of mass and size. This result is in agreement with the low-redshift results of B18 and B20 for the stellar metallicity of quiescent and star-forming galaxies respectively and D’Eugenio et al. (2018) for the gas-phase metallicity of star-forming galaxies. Our results also agree with Díaz-García et al. (2019), who showed that (at fixed mass) smaller quiescent galaxies are more metal-rich since  $z \sim 1$ . For non-zero uncertainty on  $R_e$ ,  $M_*/R_e^x$  must have a higher observational uncertainty than  $M_*$  alone (for  $x \neq 0$ ). Therefore, our result that the observed  $[Z/H]-M/R^{-1}$  relation is tighter than the relation with  $M_*$  alone means the relation with  $M/R^{-1}$  must be *intrinsically* tighter.

These studies proposed that the global stellar and gas-phase metallicity of a galaxy is regulated by the gravitational potential ( $\Phi$ ), as the depth of the potential well determines the escape velocity required for metal-rich gas to be expelled from the system by supernova, active galactic nuclei (AGN) and/or stellar winds and thus avoid being recycled into later stellar generations. Our finding that the relation also exists at  $0.60 \leq z \leq 0.76$  supports this hypothesis.

It is interesting to note that the ratio of coefficients of the best-fit planes for the three samples are all equal within  $1\sigma$ . If we simplify the complex process of metal production and outflows to a closed box model and assume the global stellar metallicity results from a balance between metal production determined by the stellar mass and metal retention determined by the gravitational potential and the strength and frequency of gas outflows, our results are consistent with there being no significant change in the balance of these processes

from  $0.014 \leq z \leq 0.76$ . While we are unable to quantitatively test this hypothesis due to differences in the sample selection between the two surveys, future works focusing on the slope and scatter of the  $[Z/H]-\Phi$  relation across redshift may shed light on this topic, and help place constraints on the strength and efficiency of feedback process in heating and expelling interstellar gas.

## 5.2 The build-up of the age– $\Sigma$ relation over 6 Gyr

Unlike the metallicity results, we find a significant difference between the age distribution in the mass–size plane at intermediate redshift compared to low redshift. B18 and B20 found that the global age of both low-redshift early-type and star-forming galaxies tightly correlates with the surface density ( $\Sigma \propto M_*/R_c^2$ ), whereas we find no significant correlation with  $\Sigma$  in either LEGA-C redshift sample. Comparing the results from the highest to lowest redshift bin, age changes from varying *along* the relation in the mass–size plane ( $0.68 < z \leq 0.76$ ), to there being no significant correlation in any direction ( $0.6 \leq z \leq 0.68$ ), to a strong variation *perpendicular* to the mass–size sequence (approximately along lines of constant  $\Sigma$ ;  $0.014 \leq z \leq 0.10$ ). This suggests that, unlike the  $[Z/H]-\Phi$  relation, the  $z \sim 0$  age– $\Sigma$  does not reflect a causal relation, but is instead built up over time due to the fact that both age and  $\Sigma$  depend on the conditions of the Universe when a galaxy becomes quiescent. We relate the change across redshift of the age dependence on mass and size, to the evolution of the mass–size plane in Section 4.3, and show that we can explain the  $z \sim 0$  age– $\Sigma$  relation as being due to the average surface density of galaxies in both the star-forming and quiescent populations decreasing with decreasing redshift.

Individual star-forming galaxies evolve along their sequence in the mass–size plane (Lilly et al. 1998; Ravindranath et al. 2004; Trujillo et al. 2006a; Pezzulli et al. 2015; van Dokkum et al. 2015), increasing in surface density as they increase in mass (Equations 6–8). Notably, the y-intercept of the star-forming sequence in the mass–size plane increases with decreasing redshift (van der Wel et al. 2014; Mowla et al. 2019), such that galaxies that formed later will be larger at fixed mass. When a star-forming galaxy quenches it joins the quiescent sequence, which has a near constant slope of  $\sim 0.5$  in the mass–size plane across redshift (Mowla et al. 2019), reflecting a sequence with constant surface density (Equations 3–5 and Figure 8). Similarly to the star-forming sequence, the y-intercept of the quiescent sequence increases with decreasing redshift. Therefore, galaxies that quenched earlier tend to do so at higher surface density. The  $z \sim 0$  quiescent and star-forming sequences are therefore built up by galaxies that have formed, evolved and quenched at a range of redshifts and therefore at a range of surface densities, leading to the  $z \sim 0$  age– $\Sigma$  relations. This hypothesis is supported by a number of key results. In particular, Kauffmann et al. (2003, 2006) and Franx et al. (2008) showed that galaxy star formation histories are strongly correlated with surface mass density. This correlation between star formation history and surface density was further refined by Díaz-García et al. (2019) and Zolotov et al. (2015), who showed that central surface density correlates strongly with formation epoch and quenching epoch respectively.

There remain two unanswered questions: (1) what leads to galaxies forming more compactly at higher redshifts? and (2) what leads to the decrease with time of the redshift-dependent threshold surface density at which star-forming galaxies quench? In relation to the first question, Franx et al. (2008) concluded that compact galaxies must have formed their stars earlier when the Universe was denser and had a higher gas fraction compared to the formation epoch of galaxies with lower surface densities. Wellons et al. (2015) used the Illustris

simulations (Genel et al. 2014; Vogelsberger et al. 2014) to trace the star-formation and assembly histories of compact galaxies and found that another dominant mechanism for forming compact galaxies at high redshift are centrally-concentrated starbursts triggered by wet major mergers. Wellons et al. (2015) noted that this wet major merger mechanism is also intrinsically linked to the density and redshift evolution of the Universe; as the Universe expanded and the abundance of cold gas decreased, the likelihood of wet major mergers also decreased with decreasing redshift. While these explanations may underlie the change in the formation and evolution of galaxies across redshift (question 1), they do not explain the origin of the redshift-dependent surface density threshold at which star-forming galaxies quench (question 2). This changing threshold may be due a redshift-dependence of the complex balance between the supply and heating of inflowing gas and the feedback and outflows from star formation and AGN (e.g., Chen et al. 2020).

## 5.3 The effect of mergers

Thus far we have only considered the evolution in the average properties of the quiescent and star-forming populations due to the addition (and loss) of new (and old) members. However individual galaxies also grow in mass and size through major and minor mergers (e.g. Oser et al. 2012; Bluck et al. 2012; Oogi & Habe 2013; Ownsworth et al. 2014). Indeed, the relative absence at low redshift of the very compact galaxies frequently observed at high redshift indicates individual galaxies must undergo significant mass–size evolution even after ceasing star formation (van Dokkum et al. 2010). Dry major mergers are expected to increase a galaxy’s mass and size proportionally, whereas minor mergers significantly increase a galaxy’s effective radius while contributing comparatively little to its stellar mass (Bezanson et al. 2009; Naab et al. 2009; Hopkins et al. 2009). Given these two relations, both major and minor mergers will increase a galaxy’s mass but *decrease* its surface mass density and therefore move galaxies down and right in the mass– $\Sigma$  plane. Specifically, based on results from Naab et al. (2009) and Bezanson et al. (2009):

$$\Delta \log R_{e,\text{major}} \approx \Delta \log M_* \quad (11)$$

$$\Delta \log R_{e,\text{minor}} \approx 2\Delta \log M_* \quad (12)$$

Therefore the changes in surface mass density are always negative (galaxies become more diffuse):

$$\Delta \log \Sigma_{\text{major}} \approx -\Delta \log M_* \quad (13)$$

$$\Delta \log \Sigma_{\text{minor}} \approx -3\Delta \log M_* \quad (14)$$

We can explore the implications of mergers on the build-up of the age–surface density relation by considering a hypothetical scenario in which galaxies quench at a surface density *independent* of redshift (i.e. there is no redshift evolution of the mass–size plane). If we consider only mass growth through mergers (i.e. no star-formation) and assume that older galaxies (those that formed earlier) will on average have undergone more mergers than younger galaxies, this would lead to older galaxies having on average a *lower* surface density than young galaxies at fixed mass—the opposite of the trend seen at  $z \sim 0$ . Therefore, while individual galaxy evolution through mergers will undoubtedly introduce scatter into the relation, it cannot be the cause of our age results; in fact, it suggests the original relation must be even stronger than observed today. In addition to increasing a galaxy’s mass and size, mergers can also restart star-formation in quenched galaxies, lowering the mean stellar population age. At  $z < 1$  10–15% of quiescent galaxies undergo rejuvenated star formation



(Thomas et al. 2010; Chauke et al. 2019), which may account for some of the intrinsic scatter in the age– $\Sigma$ .

## 6 SUMMARY AND CONCLUSIONS

We have analysed and quantified how the global stellar population parameters of age and metallicity vary in the mass–size plane between low ( $0.014 \leq z \leq 0.10$ ) and intermediate ( $0.60 \leq z \leq 0.76$ ) redshifts. Specifically, we investigate whether the  $[Z/H]-M_*/R_e$  and age– $M_*/R_e^2$  relations found at low redshift by B18 for quiescent galaxies are also present in a sample with similar masses at a look-back time of 6 Gyr. We find the  $[Z/H]-M_*/R_e$  relation is also present at intermediate redshifts but the age– $M_*/R_e^2$  relation is not.

Our conclusion that the  $[Z/H]-M_*/R_e$  also exists at  $0.60 \leq z \leq 0.76$  extends our previous results at low redshift for stars (B18; B20) and gas (D’Eugenio et al. 2018) and supports the theory that the depth of the gravitational potential well regulates the stellar and gas-phase metallicity by determining the escape velocity required for metal-rich gas to be expelled from the system and thus avoid being recycled into later stellar generations (e.g. Franx & Illingworth 1990).

To understand the change in the way age varies across the mass–size plane from low to intermediate redshift, we consider the evolution of the mass–size plane itself. Specifically, we show that the slope of  $\sim 0.5$  for the quiescent population in the mass–size plane in this redshift range (Mowla et al. 2019) leads to flat slopes in the mass–surface density plane, with an intercept that decreases with decreasing redshift. This implies that star-forming galaxies reach a redshift-dependent threshold surface density at which they quench. Importantly this threshold is higher at higher redshifts, so that galaxies forming and evolving at higher redshifts reach a higher surface density before quenching compared to low-redshift star-forming galaxies. The age–surface density relation at  $z \sim 0$  is therefore the result of the build-up of the low redshift quiescent and star-forming populations from galaxies that have formed, evolved, and quenched over a range of redshifts, and hence over a range of surface densities. Consequently, the age–surface density relation at  $z \sim 0$  arises from the cumulative effect of the redshift-dependent processes that drive the evolution of the star-forming and quiescent populations in the mass–size plane.

Future spectroscopic surveys such as MOONRISE (Maiolino et al. 2020) will help to push this relation to higher redshift ( $z \sim 1 - 2.5$ ) while the large sample size and mass range of the Hector survey (Bryant et al. 2020) at  $z \sim 0$  will allow exploration of these relations in the low-mass regime.

## 7 ACKNOWLEDGEMENTS

TMB is supported by an Australian Government Research Training Program Scholarship. FDE and AvdW acknowledge funding through from the European Research Council (ERC) under the European Union’s Horizon 2020 research and innovation program, grant agreement No. 683184. NS acknowledges the support of an Australian Research Council Discovery Early Career Research Award (project number DE190100375). JvdS acknowledges support of an Australian Research Council Discovery Early Career Research Award (project number DE200100461) funded by the Australian Government. P.F.W. acknowledges the support of the fellowship from the East Asian Core Observatories Association. RB gratefully acknowledges funding provided by the Robert C. Smith Fund and the Betsy R. Clark Fund of The Pittsburgh Foundation. LC is the recipient of an Australian

Research Council Future Fellowship (FT180100066) funded by the Australian Government. JBH is supported by an ARC Laureate Fellowship FL140100278. The SAMI instrument was funded by Bland-Hawthorn’s former Federation Fellowship FF0776384, an ARC LIEF grant LE130100198 (PI Bland-Hawthorn) and funding from the Anglo-Australian Observatory. JJB acknowledges support of an Australian Research Council Future Fellowship (FT180100231). MSO acknowledges the funding support from the Australian Research Council through a Future Fellowship (FT140100255).

This research was supported by the Australian Research Council Centre of Excellence for All Sky Astrophysics in 3 Dimensions (ASTRO 3D) through project CE170100013.

The LEGA-C Public Spectroscopy Survey observations were made with ESO Telescopes at the La Silla Paranal Observatory under program IDs 194-A.2005 and 1100.A-0949.

The SAMI Galaxy Survey is based on observations made at the Anglo-Australian Telescope. The Sydney-AAO Multi-object Integral field spectrograph (SAMI) was developed jointly by the University of Sydney and the Australian Astronomical Observatory. The SAMI input catalogue is based on data taken from the Sloan Digital Sky Survey, the GAMA Survey and the VST ATLAS Survey. The SAMI Galaxy Survey is supported by the Australian Research Council Centre of Excellence for All Sky Astrophysics in 3 Dimensions (ASTRO 3D) through project number CE170100013, the Australian Research Council Centre of Excellence for All-sky Astrophysics (CAASTRO), through project number CE110001020, and other participating institutions. The SAMI Galaxy Survey website is <http://sami-survey.org/>.

We acknowledge the traditional custodians of the land on which the AAT stands, the Gamilaraay people, and pay our respects to their elders past, present and emerging.

This research was conducted using the freely available PYTHON programming language (Van Rossum & Drake Jr 1995), maintained and distributed by the Python Software Foundation, and the IPYTHON extension (Perez & Granger 2007). Our analysis made use of the NUMPY (van der Walt et al. 2011), SCIPY (Virtanen et al. 2020), ASTROPY (Astropy Collaboration et al. 2013), MATPLOTLIB (Hunter 2007), and CORNER (Foreman-Mackey 2016) packages. In preliminary analyses, we also used TOPCAT (Taylor 2005) and NED WRIGHT’S COSMOLOGY CALCULATOR (Wright 2006). We make extensive use of NASA’s Astrophysics Data System.

## DATA AVAILABILITY

The SAMI data used in this work is publically available and hosted on the Australian Astronomical Optics’ Data Central (<https://datacentral.org.au/> Croom et al. 2021a). The LEGA-C data used is in the public domain via the ESO Science Archive and through the Mikulski Archive for Space Telescopes (MAST). The full reduced data set will be available in the upcoming third public data release. Part of the reduced data is available on the LEGA-C website (Straatman et al. 2018).

## REFERENCES

- Abazajian K. N., et al., 2009, *ApJS*, 182, 543  
 Abramson L. E., Gladders M. D., Dressler A., Oemler Augustus J., Poggianti B., Vulcani B., 2016, *ApJ*, 832, 7  
 Allen J. T., et al., 2015, *MNRAS*, 446, 1567  
 Almaini O., et al., 2017, *MNRAS*, 472, 1401  
 Andrews S. K., Driver S. P., Davies L. J. M., Kafle P. R., Robotham A. S. G., Wright A. H., 2017, *MNRAS*, 464, 1569

- Astropy Collaboration et al., 2013, *A&A*, 558, A33
- Balogh M. L., Morris S. L., Yee H. K. C., Carlberg R. G., Ellingson E., 1999, *ApJ*, 527, 54
- Barone T. M., et al., 2018, *ApJ*, 856, 64
- Barone T. M., D'Eugenio F., Colless M., Scott N., 2020, *ApJ*, 898, 62
- Barro G., et al., 2013, *ApJ*, 765, 104
- Bell E. F., de Jong R. S., 2000, *MNRAS*, 312, 497
- Bell E. F., Barnaby D., Bower R. G., de Jong R. S., Harper D. A., Hereld M., Loewenstein R. F., Rauscher B. J., 2000, *MNRAS*, 312, 470
- Bezanson R., van Dokkum P. G., Tal T., Marchesini D., Kriek M., Franx M., Coppi P., 2009, *ApJ*, 697, 1290
- Bland-Hawthorn J., et al., 2011, *Optics Express*, 19, 2649
- Bluck A. F. L., Conselice C. J., Buitrago F., Grützbauch R., Hoyos C., Mortlock A., Bauer A. E., 2012, *ApJ*, 747, 34
- Bruzual G., Charlot S., 2003, *MNRAS*, 344, 1000
- Bryant J. J., Bland-Hawthorn J., Fogarty L. M. R., Lawrence J. S., Croom S. M., 2014, *MNRAS*, 438, 869
- Bryant J. J., et al., 2015, *MNRAS*, 447, 2857
- Bryant J. J., et al., 2020, in Society of Photo-Optical Instrumentation Engineers (SPIE) Conference Series. p. 1144715, doi:10.1117/12.2560309
- Buitrago F., Trujillo I., Conselice C. J., Bouwens R. J., Dickinson M., Yan H., 2008, *ApJ*, 687, L61
- Calzetti D., Armus L., Bohlin R. C., Kinney A. L., Koornneef J., Storchi-Bergmann T., 2000, *ApJ*, 533, 682
- Cappellari M., 2017, *MNRAS*, 466, 798
- Cappellari M., Emsellem E., 2004, *PASP*, 116, 138
- Cappellari M., et al., 2013a, *MNRAS*, 432, 1862
- Cappellari M., et al., 2013b, *MNRAS*, 432, 1709
- Carollo C. M., et al., 2013, *ApJ*, 773, 112
- Chabrier G., 2003, *PASP*, 115, 763
- Charlot S., Fall S. M., 2000, *ApJ*, 539, 718
- Chauke P., et al., 2018, *ApJ*, 861, 13
- Chauke P., et al., 2019, *ApJ*, 877, 48
- Chen Z., et al., 2020, *ApJ*, 897, 102
- Cleveland W. S., Devlin S. J., 1988, *Journal of the American Statistical Association*, 83, 596
- Croom S. M., et al., 2012, *MNRAS*, 421, 872
- Croom S. M., et al., 2021a, arXiv e-prints, p. arXiv:2101.12224
- Croom S. M., et al., 2021b, arXiv e-prints, p. arXiv:2105.10179
- D'Eugenio F., Colless M., Groves B., Bian F., Barone T. M., 2018, *MNRAS*, 479, 1807
- D'Eugenio F., et al., 2020, *MNRAS*, 497, 389
- Daddi E., et al., 2007, *ApJ*, 670, 156
- Daddi E., et al., 2010, *ApJ*, 713, 686
- Davies L. J. M., et al., 2015, *MNRAS*, 447, 1014
- Díaz-García L. A., et al., 2019, *A&A*, 631, A158
- Dopita M. A., Sutherland R. S., 2003, *Astrophysics of the diffuse universe*. Springer
- Dressler A., Gunn J. E., 1983, *ApJ*, 270, 7
- Dressler A., Smail I., Poggianti B. M., Butcher H., Couch W. J., Ellis R. S., Oemler Augustus J., 1999, *ApJS*, 122, 51
- Driver S. P., et al., 2011, *MNRAS*, 413, 971
- Driver S. P., et al., 2018, *MNRAS*, 475, 2891
- Edge A., Sutherland W., Kuijken K., Driver S., McMahon R., Eales S., Emerson J. P., 2013, *The Messenger*, 154, 32
- Epinat B., et al., 2012, *A&A*, 539, A92
- Faisst A. L., Carollo C. M., Capak P. L., Tacchella S., Renzini A., Ilbert O., McCracken H. J., Scoville N. Z., 2017, *ApJ*, 839, 71
- Ferguson H. C., et al., 2004, *ApJ*, 600, L107
- Foreman-Mackey D., 2016, *The Journal of Open Source Software*, 1, 24
- Foreman-Mackey D., Hogg D. W., Lang D., Goodman J., 2013, *PASP*, 125, 306
- Förster Schreiber N. M., et al., 2006, *ApJ*, 645, 1062
- Förster Schreiber N. M., et al., 2009, *ApJ*, 706, 1364
- Franx M., Illingworth G., 1990, *ApJ*, 359, L41
- Franx M., van Dokkum P. G., Förster Schreiber N. M., Wuyts S., Labbé I., Toft S., 2008, *ApJ*, 688, 770
- Genel S., et al., 2014, *MNRAS*, 445, 175
- Girardi L., Bressan A., Bertelli G., Chiosi C., 2000, *A&AS*, 141, 371
- González Delgado R. M., et al., 2014a, *A&A*, 562, A47
- González Delgado R. M., et al., 2014b, *ApJ*, 791, L16
- González Delgado R. M., et al., 2015, *A&A*, 581, A103
- Goodman J., Weare J., 2010, *Communications in Applied Mathematics and Computational Science*, Vol.~5, No.~1, p.~65-80, 2010, 5, 65
- Green A. W., et al., 2018, *MNRAS*, 475, 716
- Gupta A., Tran K.-V., Pillepich A., Yuan T., Harshan A., Rodriguez-Gomez V., Genel S., 2021, *ApJ*, 907, 95
- Hill D. T., et al., 2011, *MNRAS*, 412, 765
- Hill A. R., et al., 2017, *ApJ*, 837, 147
- Hopkins P. F., Bundy K., Murray N., Quataert E., Lauer T. R., Ma C.-P., 2009, *MNRAS*, 398, 898
- Hunter J. D., 2007, *Computing In Science & Engineering*, 9, 90
- Jeffreys H., 1946, *Proc. R. Soc. Lond.*, 186, 453-461
- Kassin S. A., et al., 2012, *ApJ*, 758, 106
- Kauffmann G., et al., 2003, *MNRAS*, 341, 54
- Kauffmann G., Heckman T. M., De Lucia G., Brinchmann J., Charlot S., Tremonti C., White S. D. M., Brinkmann J., 2006, *MNRAS*, 367, 1394
- Kelvin L. S., et al., 2012, *MNRAS*, 421, 1007
- Kriek M., van Dokkum P. G., Franx M., Illingworth G. D., Magee D. K., 2009, *ApJ*, 705, L71
- Labbé I., et al., 2005, *ApJ*, 624, L81
- Law D. R., Steidel C. C., Erb D. K., Larkin J. E., Pettini M., Shapley A. E., Wright S. A., 2007, *ApJ*, 669, 929
- Law D. R., Steidel C. C., Erb D. K., Larkin J. E., Pettini M., Shapley A. E., Wright S. A., 2009, *ApJ*, 697, 2057
- Le Fèvre O., et al., 2003, in Iye M., Moorwood A. F. M., eds, Society of Photo-Optical Instrumentation Engineers (SPIE) Conference Series Vol. 4841, Instrument Design and Performance for Optical/Infrared Ground-based Telescopes. pp 1670-1681, doi:10.1117/12.460959
- Leslie S. K., et al., 2020, *ApJ*, 899, 58
- Li H., et al., 2018, *MNRAS*, 476, 1765
- Lilly S. J., Le Fevre O., Hammer F., Crampton D., 1996, *ApJ*, 460, L1
- Lilly S., et al., 1998, *ApJ*, 500, 75
- Madau P., Dickinson M., 2014, *ARA&A*, 52, 415
- Madau P., Pozzetti L., Dickinson M., 1998, *ApJ*, 498, 106
- Maiolino R., et al., 2020, *The Messenger*, 180, 24
- McCracken H. J., et al., 2012, *A&A*, 544, A156
- McDermid R. M., et al., 2015, *MNRAS*, 448, 3484
- Medling A. M., et al., 2018, *MNRAS*, 475, 5194
- Moles M., et al., 2008, *AJ*, 136, 1325
- Møller P., Christensen L., 2020, *MNRAS*, 492, 4805
- Morokuma-Matsui K., Baba J., 2015, *MNRAS*, 454, 3792
- Mowla L. A., et al., 2019, *ApJ*, 880, 57
- Muzzin A., et al., 2013a, *ApJS*, 206, 8
- Muzzin A., et al., 2013b, *ApJ*, 777, 18
- Naab T., Johansson P. H., Ostriker J. P., 2009, *ApJ*, 699, L178
- Oogi T., Habe A., 2013, *MNRAS*, 428, 641
- Oser L., Naab T., Ostriker J. P., Johansson P. H., 2012, *ApJ*, 744, 63
- Osterbrock D. E., Ferland G. J., 2006, *Astrophysics of gaseous nebulae and active galactic nuclei*. University Science Books
- Owers M. S., et al., 2017, *MNRAS*, 468, 1824
- Ownsworth J. R., Conselice C. J., Mortlock A., Hartley W. G., Almaini O., Duncan K., Mundy C. J., 2014, *MNRAS*, 445, 2198
- Peng C. Y., Ho L. C., Impey C. D., Rix H.-W., 2010, *AJ*, 139, 2097
- Perez F., Granger B. E., 2007, *Computing in Science Engineering*, 9, 21
- Pezzulli G., Fraternali F., Boissier S., Muñoz-Mateos J. C., 2015, *MNRAS*, 451, 2324
- Pietrinferni A., Cassisi S., Salaris M., Castelli F., 2004, *ApJ*, 612, 168
- Pietrinferni A., Cassisi S., Salaris M., Castelli F., 2006, *ApJ*, 642, 797
- Pillepich A., et al., 2018, *MNRAS*, 475, 648
- Ravindranath S., et al., 2004, *ApJ*, 604, L9
- Renzini A., Peng Y.-j., 2015, *ApJ*, 801, L29
- Sánchez-Blázquez P., et al., 2006, *MNRAS*, 371, 703
- Scott N., et al., 2009, *MNRAS*, 398, 1835
- Scott N., et al., 2017, *MNRAS*, 472, 2833
- Scott N., et al., 2018, *MNRAS*, 481, 2299

- Scoville N., et al., 2007, *ApJS*, 172, 38
- Sersic J. L., 1968, Atlas de Galaxias Australes. Observatorio Astronomico, Universidad Nacional de Cordoba
- Sharp R., et al., 2006, in Society of Photo-Optical Instrumentation Engineers (SPIE) Conference Series. p. 62690G ([arXiv:astro-ph/0606137](https://arxiv.org/abs/astro-ph/0606137)), [doi:10.1117/12.671022](https://doi.org/10.1117/12.671022)
- Sharp R., et al., 2015, *MNRAS*, 446, 1551
- Speagle J. S., Steinhardt C. L., Capak P. L., Silverman J. D., 2014, *ApJS*, 214, 15
- Storn R., Price K., 1997, *Journal of Global Optimization*, 11, 341
- Stott J. P., et al., 2016, *MNRAS*, 457, 1888
- Straatman C. M. S., et al., 2018, *ApJS*, 239, 27
- Sutherland W., et al., 2015, *A&A*, 575, A25
- Swinbank A. M., Smail I., Sobral D., Theuns T., Best P. N., Geach J. E., 2012, *ApJ*, 760, 130
- Tacconi L. J., et al., 2010, *Nature*, 463, 781
- Tacconi L. J., et al., 2013, *ApJ*, 768, 74
- Taylor M. B., 2005, in Shopbell P., Britton M., Ebert R., eds, *Astronomical Society of the Pacific Conference Series Vol. 347, Astronomical Data Analysis Software and Systems XIV*. p. 29
- Thomas D., Maraston C., Schawinski K., Sarzi M., Silk J., 2010, *MNRAS*, 404, 1775
- Trujillo I., et al., 2006a, *Monthly Notices of the Royal Astronomical Society: Letters*, 373, 36
- Trujillo I., et al., 2006b, *ApJ*, 650, 18
- Trujillo I., Conselice C. J., Bundy K., Cooper M. C., Eisenhardt P., Ellis R. S., 2007, *MNRAS*, 382, 109
- Van Rossum G., Drake Jr F. L., 1995, *Python reference manual*. Centrum voor Wiskunde en Informatica Amsterdam
- Vazdekis A., Sánchez-Blázquez P., Falcón-Barroso J., Cenarro A. J., Beasley M. A., Cardiel N., Gorgas J., Peletier R. F., 2010, *MNRAS*, 404, 1639
- Virtanen P., et al., 2020, *Nature Methods*, 17, 261
- Vogelsberger M., et al., 2014, *MNRAS*, 444, 1518
- Wake D. A., van Dokkum P. G., Franx M., 2012, *ApJ*, 751, L44
- Weiner B. J., et al., 2006, *ApJ*, 653, 1027
- Wellons S., et al., 2015, *MNRAS*, 449, 361
- Whitaker K. E., van Dokkum P. G., Brammer G., Franx M., 2012, *ApJ*, 754, L29
- Whitaker K. E., et al., 2017, *ApJ*, 838, 19
- Williams R. J., Quadri R. F., Franx M., van Dokkum P., Toft S., Kriek M., Labbé I., 2010, *ApJ*, 713, 738
- Wisnioski E., et al., 2011, *MNRAS*, 417, 2601
- Wisnioski E., et al., 2015, *ApJ*, 799, 209
- Wisnioski E., et al., 2019, *ApJ*, 886, 124
- Wright E. L., 2006, *PASP*, 118, 1711
- Wright S. A., Larkin J. E., Law D. R., Steidel C. C., Shapley A. E., Erb D. K., 2009, *ApJ*, 699, 421
- Wu P.-F., et al., 2018, *ApJ*, 868, 37
- Wu P.-F., et al., 2020, *ApJ*, 888, 77
- Wuyts S., et al., 2011, *ApJ*, 742, 96
- Yano M., Kriek M., van der Wel A., Whitaker K. E., 2016, *ApJ*, 817, L21
- Zibetti S., Gallazzi A. R., Hirschmann M., Consolandi G., Falcón-Barroso J., van de Ven G., Lyubenova M., 2020, *MNRAS*, 491, 3562
- Zolotov A., et al., 2015, *MNRAS*, 450, 2327
- da Cunha E., Charlot S., Elbaz D., 2008, *MNRAS*, 388, 1595
- de Graaff A., et al., 2020, *ApJ*, 903, L30
- de Graaff A., et al., 2021, arXiv e-prints, p. [arXiv:2103.12753](https://arxiv.org/abs/2103.12753)
- van Dokkum P. G., Franx M., 2001, *ApJ*, 553, 90
- van Dokkum P. G., et al., 2010, *ApJ*, 709, 1018
- van Dokkum P. G., et al., 2015, *ApJ*, 813, 23
- van der Walt S., Colbert S. C., Varoquaux G., 2011, *Computing in Science Engineering*, 13, 22
- van der Wel A., Bell E. F., van den Bosch F. C., Gallazzi A., Rix H.-W., 2009, *ApJ*, 698, 1232
- van der Wel A., et al., 2012, *ApJS*, 203, 24
- van der Wel A., et al., 2014, *ApJ*, 788, 28
- van der Wel A., et al., 2016, *ApJS*, 223, 29

This paper has been typeset from a  $\text{\TeX}/\text{\LaTeX}$  file prepared by the author.